Feasibility Investigations of Swing-Assist Knee Prosthesis and Cold-Gas Thruster based Fall Prevention Device

By

Almaskhan Baimyshev

Dissertation

Submitted to the Faculty of the

Graduate School of Vanderbilt University

in partial fulfillment of the requirements

for the degree of

DOCTOR OF PHILOSOPHY

in

Mechanical Engineering

May 31, 2022

Nashville, Tennessee

Approved:

Michael Goldfarb, Ph.D.

David Braun, Ph.D.

Kenneth Frampton, Ph.D.

Nilanjan Sarkar, Ph.D.

Robert Pitz, Ph.D.

DEDICATON

To my mother, Elvira,
and my little brother, Amankhan,
for their infinite love and support.

ACKNOWLEDGEMENTS

The work presented in this dissertation would not have been possible without the help and support of many people. First of all, I would like to thank Dr. Michael Goldfarb, an engineering expert and an excellent mentor. I am grateful for his guidance, trust, and continuous encouragement. I would also like to express my gratitude to Dr. Nilanjan Sarkar, Dr. David Braun, Dr. Robert Pitz, and Dr. Kenneth Frampton for serving as members of my dissertation committee and helping me make my research the best it could have been.

I would like to thank Dr. Brian Lawson for his guidance during my work on the Swing-Assist Knee, Leo Vailati and Don Truex for their help with electronics, Steve Culver and Dr. Ben Gasser for helping me with machining, and Shane King and Maura Eveld for their help with collecting and processing motion capture data. Big thanks to Jantzen Lee and Amanda Shultz for allowing me to use the embedded systems they have designed. I am also very thankful to have collaborated with Michael Finn-Henry on the Cold-Gas Thruster. His design and machining skills along with his cheerfulness and tirelessness were invaluable during my work.

My thanks to all members of the Center for Rehabilitation Engineering and Assistive Technology (CREATe), who created a friendly and enjoyable work environment.

TABLE OF CONTENTS

Page

LIST OF FIGURES

LIST OF TABLES

CHAPTER 1

INTRODUCTION

This dissertation consists of two parts that explore the viability of two prospective wearable mechatronic devices. The first part is a preliminary investigation of the prospective value of a low-powered, low-impedance, swing-assist knee prosthesis concept. The proposed device employs a smaller motor, transmission, and battery than existing powered knee prostheses, which enables construction with a lower output impedance, and implementation in a smaller, lighter, and quieter package. Since the prototype is intended to explore the value of swing assistance, stance-phase stability for the prototype is provided by the knee hyperextension stop. The underlying hypothesis of the swing-assist concept is that a passive, low-output impedance knee provides desirable behavior (i.e., is highly receptive to user input), but lacks positional robustness during swing-phase, particularly in the presence of perturbations. The Swing Assist (SA) knee can assist the user with swing initiation and potentially reject swing phase disturbances, such as underpowered swing initiation, scuffing, and stumble, while maintaining a highly consistent knee angle profile and cadence adaptivity. In order to assess the prospective value and functionality of a swing-assist concept, a prototype was constructed with a controller configured to provide low-impedance swing with swing-assist functionality.

The second part of this dissertation is a feasibility exploration of a cold-gas thruster (CGT) based wearable fall prevention device. The CGT is an electronically controlled cold-gas thruster, intended as a backpack-worn device for backward fall prevention for individuals at fall risk. The device is comprised of a pressurized air tank combined with a custom electrically actuated high-flow-capacity valve and servo-controlled nozzle, which are employed together to create a thrust to restore balance in instances of an impending fall. The intent of the research associated with the CGT is to assess the prospective efficacy of a CGT-type device in potentially correcting an impending fall. This research involved performing design calculations; designing a

prototype system to provide appropriate thrust characteristics; designing a supervisory controller to detect impending falls and provide corrective force at an appropriate time; and testing the device on an experimental analog to a human user. For feasibility experiments, a rocking block apparatus was configured to have physical parameters similar to those of a standing human. A notable property of this apparatus is that a rocking block has a range of inclinations from which it can return to stability, as opposed to the inverted pendulum model, which has a single point of equilibrium. The boundaries of this safe range are approximately analogous to a standing person's limits of stability (LOS). This experimental apparatus was used to quantify the control authority of the constructed CGT prototype and to assess the real-time autonomous supervisory controller, developed to detect and prevent impending falls by applying the CGT-generated assistive thrust.

1. Swing-Assist Knee

There are approximately 600,000 persons living in the US with major lower limb amputation, approximately half of whom have transfemoral amputation (TFA) [1]. The worldwide prevalence of TFA is approximately 20-30 times the US prevalence [2].

Multiple types of knee prostheses exist to help restore legged mobility to individuals with TFA [3]. The two primary functions of a knee prosthesis are to provide support (called stance control) during the stance phase of walking and to provide appropriate motion during the swing phase. Traditional passive prostheses typically provide stance phase stability via a hyperextension stop which is engaged by a combination of hip torque and ground reaction force. In some passive prostheses, knee stability during stance is further supplemented by the introduction of stance phase damping, either engaged by microprocessor control (e.g., C-leg) or by mechanical sensing of stance phase (e.g., Mauch knee).

The essential aspects of swing phase are sufficient knee flexion to assure toe clearance (i.e., to avoid scuffing the ground during swing) and subsequent sufficient knee extension, which is necessary to achieve knee stability for the following stance

phase. Passive knee prostheses achieve swing-phase motion by providing a low resistance which, when combined with the (active) swing phase movement of the residual thigh, in combination with the inertial properties of the lower leg, results in an initial swing-phase knee flexion, followed by knee extension. In some microprocessor-controlled knees (MPKs), swing knee resistance is modulated as a function of walking cadence. In all cases of passive prostheses (i.e., non-MPK and MPK), swing phase is resistive. Since knee extension at the swing completion is imperative, many passive knee prostheses employ an "extension aid" which is essentially a spring that helps promote full knee extension. Such an extension aid, however, opposes knee flexion and therefore promotes late-swing knee extension at the expense of limiting mid-swing knee flexion. In all passive prostheses, achieving proper swing-phase knee motion is an open-loop process – the user must provide the appropriate thigh motion to achieve a desired motion through the passive dynamics of the leg. As with all open-loop systems, the output of the system (in this case the motion of the knee) is sensitive to disturbances (e.g., scuffing or stumbling), and also sensitive to changes in the model, such as those that might occur as a result in changes footwear, ground slope, or environmental temperature. This lack of robustness is further exacerbated by the lack of proprioception at the prosthetic knee.

In order to address some of the deficiencies of passive prostheses, prostheses with powered joints (e.g., Power Knee) have been developed. The recent review [4] enumerates over 20 powered prosthesis prototypes (e.g., [5-7]). Powered knee prostheses typically utilize a motor and drive system to provide both stance-phase support and swing phase motion at the knee. In doing so, the swing phase motion can be driven to a specific trajectory, and therefore the swing-phase motion can be substantially more robust relative to passive prostheses. Furthermore, since the physical behavior of powered prostheses is largely software-programmable, they are able to offer a wide range of biomechanical functionality and thus can better adapt their behavior to various activities and terrain relative to passive prostheses [8]. Despite these advantages, the requirements of substantial joint torque and power associated

with stance-phase activities in particular generally result in larger, heavier, and noisier prostheses relative to passive counterparts.

Chapter 1 of this dissertation proposes a hybrid approach to providing stance and swing control in which stance control is provided strictly by passive means, but swing control utilizes a small motor for assistance. The approach is therefore called a Swing Assist (SA) knee. The motor is a form of "extension aid" in a passive knee; rather than providing strictly extension, however, the motor is able to aid both flexion in mid swing and extension in late swing. The SA prosthesis is intended to inject small amounts of power during the swing phase in order to guide the knee through a swing trajectory. Since the assistance is associated with low-torque and low-power movements, the motor, transmission, and battery can be small, lightweight, and quiet relative to a fully-powered knee prosthesis. This paper describes a device prototype intended to explore the potential efficacy of an SA prosthesis; describes the prosthesis controller; and describes experiments on a single individual with transfemoral amputation (ITFA) that compares swing-phase characteristics provided by the SA knee with those of a commercially-available MPK.

2. Cold-Gas Thruster

Falls in elderly people are a well-known cause of injury. One in four people over the age of 65 fall every year costing an estimated $31.3 billion to Medicare annually [9]. As people age, their balance declines due to several physiological changes. In particular, balance depends on visual, vestibular, proprioceptive, and musculoskeletal systems, all of which are subject to become compromised as age advances [10]. Falls can lead to severe injuries, fear of falling, loss of independence and death [11]. The majority of fall prevention research has focused on in-home strategies for preventing falls, such as handrails, higher friction flooring, and improved lighting. However, an epidemiological study of falls in older community-dwellings showed that 62% of falls occur while outside of the home [12]. A significant unmet need exists for a device to prevent falls outside of the home without a large impact on the user's lifestyle.

The recent emergence of wearable devices may offer promise to aid fall prevention. At this point, relatively little research exists on the use of wearable devices for fall prevention. Although not directly related, one research group recently embedded balance control into a lower limb exoskeleton, and demonstrated the ability of a healthy individual to walk in it without requiring external balance aids [13]. This control system, however, was not intended as a fall prevention device, per se. Using lower body exoskeletons to prevent falls is challenging, since a device collocated with the lower limbs must coordinate a reactive response with the user, without otherwise interfering with the user's efforts to react to a state of imbalance. Such coordination would entail a number of challenges, including incorporating a sufficient number of actuated deg of freedom, and correctly predicting which of several possible recovery strategies an individual might choose [14-15].

A different approach is to exert a body force or moment directly to the human body (rather than act through the lower limbs), which decouples the corrective action of the force or moment from movement of the limbs. In this way, such a system could assist balance without interfering with the user's ability to use his or her lower limb to correct for imbalance. In an effort to assist balance, without interfering with the movement of the lower limbs, some researchers have employed control moment gyroscopes (CMGs) to impose controllable torques directly to a user's trunk [16-19]. This approach is a "reactionless" approach, since it creates a moment relative to the inertial reference frame (IRF) rather than by direct contact with the earth. As described in detailed investigations [16-19], the approach has substantial promise to assist with recovery from states of imbalance. This approach, however, entails some limitations. First, these devices are not able to apply forces to the trunk (i.e., they apply moments). Second, there is a design trade-off between the size of the device, the rotational speed at which the flywheels must rotate, the mass of the flywheels, and the magnitude of the resulting torque, which together requires a careful trade between size, weight, vibration, audible noise, quiescent power consumption, and magnitude of achievable control moment impulse.

An alternate means of imposing a reactionless force on an individual's trunk or body is via a thruster. A cold-gas thruster (CGT) typically employs a compressed gas, such as nitrogen or CO_2, which flows through a nozzle, to produce a force relative to the IRF via the rate of change of momentum of the gas. The characteristics of a given force impulse can be influenced by gas pressure and molecular weight, and nozzle characteristics. In addition to providing a reactionless force, as opposed to a moment, relative to a CMG, a CGT may result in a lighter-weight device, since the fundamental source of momentum is a gas contained in a pressure vessel. Also, a CGT would require no significant quiescent power and entail no quiescent noise; however, it will surely generate noise when thrusting. For these reasons, a cold gas thruster may be a viable alternative to CMGs for fall prevention.

The extent to which a CGT might be viable as a backpack-worn balance assistance device is unclear. In this application, the CGT system would sense a pending fall and increase the margin of stability by counteracting such falls with a burst of thrust that returns the person to their region of stability. Such an approach is only viable if the CGT provides suitable control authority to restore balance (i.e., increase the margin of stability). Chapters 2 and 3 are intended to address this feasibility question – namely, to investigate the extent to which a CGT of reasonable design parameters can increase margin of stability of a falling person. In order to address this feasibility question, the authors employed modeling and simulation to assess the design feasibility; designed and constructed a CGT prototype; designed and employed a rocking block as an approximate model of a standing human; developed a real-time autonomous supervisory controller; conducted experiments to verify the corrective characteristics of the CGT prototype.

3. Contributions

3.1. Chapter 2 Contributions

In this chapter, a novel low-power approach to knee prosthetics was explored and assessed. Using this approach, a lightweight swing-assist knee prototype was

designed and constructed. Subsequent experiments revealed that such a device has a potential to significantly reduce the user effort and improve the robustness of the prosthesis, while retaining the size and weight of a passive knee.

The contribution associated with this research included the design and construction of the swing-assist knee prototype, development of the state-machine-based controller, testing of the prototype on an individual with transfemoral amputation, and comparison of the prototype performance and the participant's daily-use prosthesis (a Rheo knee). The potential benefits of a swing-assist prosthesis to transfemoral prosthesis users were explored and a foundation was laid for continuing research that combines swing assist functionality with stance-controlled behaviors. Specifically, this research was followed by development of two swing-assist prosthesis currently being explored, one augmented by a stance phase damper in a form of hydraulic cylinder [20], and another that employs a motor with a two-speed variable transmission [21]. I presented the results of this study at the 2018 40th Annual International Conference of the IEEE Engineering in Medicine and Biology Society (EMBC) as first author.

3.2. Chapter 3 Contributions

This chapter presents the design and initial testing of a novel cold-gas thruster (CGT) based backward fall prevention device. As opposed to existing balance-maintaining assistive devices, such as exoskeletons or control moment gyroscopes, and impact-softening devices, such as inflatable hip and head protectors, this device is aimed to assist the user to recover balance after a user has entered a falling state. The CGT uses compressed gas to produce a force vector in the inertial frame of reference in a manner a human assistant would provide a restoring force to a falling person via a gait belt.

The contributions of this chapter include an analytical exploration of forces necessary to restore balance to a person falling backwards, the development of the thruster model that informed the design of the CGT prototype, the model-based nozzle controller, and testing of the prototype and the controller on a rocking block apparatus. These experiments confirmed the potential of the CGT to prevent imminent falls and

quantified the extents of the control authority of the device at zero initial velocity. The paper on this study is currently under review for publication in the Journal of Dynamic Systems, Measurement and Control. Preliminary results of this study were presented at the 2020 8th IEEE RAS/EMBS International Conference for Biomedical Robotics and Biomechatronics (BioRob) [22].

3.3. Chapter 4 Contributions

The focus of this chapter is to expand the controller and operational conditions of the CGT to include dynamic fall conditions (i.e., impending falls with non-zero initial velocity), and to experimentally validate the efficacy on a rocking block experimental apparatus. A real-time supervisory controller was developed to detect imbalance in the rocking block apparatus and to trigger the assistive thrust when appropriate. The control authority of the CGT was identified in phase space through simulations and confirmed experimentally. Additional simulations were performed to assess the CGT in context of a multi-segment human body, and some remarks on how the CGT controller should be adapted for use with human users were provided.

The contributions of this chapter include the development of the autonomous supervisory controller, the design and construction of a new version of the rocking block apparatus that more closely represents a human body, and exploration of fall prevention through a series of fall-simulating experiments. Simulations and analysis were also performed to explore the effect of the CGT on a multi-segment human body. The results of this study will be submitted to a peer-reviewed scientific journal.

4. References

[1] K. Ziegler-Graham, E. MacKenzie, P. Ephraim, T. Travison and R. Brookmeyer, "Estimating the Prevalence of Limb Loss in the United States: 2005 to 2050", *Arch Phys Med Rehabil*, vol. 89, no. 3, pp. 422-429, 2008.

[2] R. Renzi, N. Unwin, R. Jubelirer and L. Haag, "An International Comparison of Lower Extremity Amputation Rates", *Annals of Vascular Surgery*, vol. 20, no. 3, pp. 346-350, 2006.

[3] Romo, H.D. “Prosthetic knees.” *Phys Med Rehabil Clin N Am*, vol. 11, no. 3, pp. 595–607, 2000

[4] M. Windrich, M. Grimmer, O. Christ, S. Rinderknecht and P. Beckerle, "Active lower limb prosthetics: a systematic review of design issues and solutions", *BioMedical Engineering OnLine*, vol. 15, no. 3, 2016.

[5] F. Sup, A. Bohara and M. Goldfarb, "Design and Control of a Powered Transfemoral Prosthesis", *The International Journal of Robotics Research*, vol. 27, no. 2, pp. 263-273, 2008.

[6] B. Lambrecht and H. Kazerooni, "Design of a semi-active knee prosthesis", *2009 IEEE International Conference on Robotics and Automation*, 2009.

[7] E. Rouse, L. Mooney and H. Herr, "Clutchable series-elastic actuator: Implications for prosthetic knee design", *The International Journal of Robotics Research*, vol. 33, no. 13, pp. 1611-1625, 2014.

[8] M. Goldfarb, B. Lawson and A. Shultz, "Realizing the Promise of Robotic Leg Prostheses", *Science Translational Medicine*, vol. 5, no. 210, pp. 210ps15-210ps15, 2013.

[9] G. Bergen, M. R. Stevens, and E. R. Burns, “Falls and Fall Injuries Among Adults Aged ≥65 Years — United States, 2014,” *MMWR Morb. Mortal. Wkly. Rep.*, vol. 65, no. 37, pp. 993–998, Sep. 2016, doi: 10.15585/mmwr.mm6537a2.

[10] T. E. Lockhart, J. L. Smith, and J. C. Woldstad, “Effects of Aging on the Biomechanics of Slips and Falls,” *Hum. Factors J. Hum. Factors Ergon. Soc.*, vol. 47, no. 4, pp. 708–729, Dec. 2005, doi: 10.1518/001872005775571014.

[11] A. F. Ambrose, G. Paul, and J. M. Hausdorff, “Risk factors for falls among older adults: a review of the literature,” *Maturitas*, vol. 75, no. 1, pp. 51–61, May 2013, doi: 10.1016/j.maturitas.2013.02.009.

[12] S. R. Lord, J. A. Ward, P. Williams, and K. J. Anstey, “An epidemiological study of falls in older community-dwelling women: the Randwick falls and fractures

study," *Aust. J. Public Health*, vol. 17, no. 3, pp. 240–245, Sep. 1993, doi: 10.1111/j.1753-6405.1993.tb00143.x.

[13] S. Wang *et al.*, "Design and Control of the MINDWALKER Exoskeleton," *IEEE Trans. Neural Syst. Rehabil. Eng.*, vol. 23, no. 2, pp. 277–286, Mar. 2015, doi: 10.1109/TNSRE.2014.2365697.

[14] C. Shirota, A. M. Simon, and T. A. Kuiken, "Recovery strategy identification throughout swing phase using kinematic data from the tripped leg," *2014 36th Annual International Conference of the IEEE Engineering in Medicine and Biology Society*, Chicago, IL, 2014, pp. 6199–6202, doi: 10.1109/EMBC.2014.6945045.

[15] A. K. Bourke and G. M. Lyons, "A threshold-based fall-detection algorithm using a bi-axial gyroscope sensor," *Med. Eng. Phys.*, vol. 30, no. 1, pp. 84–90, Jan. 2008, doi: 10.1016/j.medengphy.2006.12.001.

[16] J. Chiu and A. Goswami, "Design of a Wearable Scissored-Pair Control Moment Gyroscope (SP-CMG) for Human Balance Assist," *Volume 5A: 38th Mechanisms and Robotics Conference*, Buffalo, New York, USA, 2014, p. V05AT08A023, doi: 10.1115/DETC2014-35539.

[17] D. Lemus, J. van Frankenhuyzen, and H. Vallery, "Design and Evaluation of a Balance Assistance Control Moment Gyroscope," *J. Mech. Robot.*, vol. 9, no. 5, p. 051007, Oct. 2017, doi: 10.1115/1.4037255.

[18] D. Li and H. Vallery, "Gyroscopic assistance for human balance," *2012 12th IEEE International Workshop on Advanced Motion Control (AMC)*, Sarajevo, Bosnia and Herzegovina, 2012, pp. 1–6, doi: 10.1109/AMC.2012.6197144.

[19] R. Matsuzaki and Y. Fujimoto, "Walking assist device using Control Moment Gyroscopes," *IECON 2013 - 39th Annual Conference of the IEEE Industrial Electronics Society*, Vienna, Austria, 2013, pp. 6581–6586, doi: 10.1109/IECON.2013.6700220.

[20] J. T. Lee, H. L. Bartlett and M. Goldfarb, "Design of a Semipowered Stance-Control Swing-Assist Transfemoral Prosthesis," *IEEE/ASME Transactions on Mechatronics*, vol. 25, no. 1, pp. 175-184, Feb. 2020, doi: 10.1109/TMECH.2019.2952084.

[21] S. Culver, L. G. Vailati, and M. Goldfarb. “Design of an electric-motor-based modulated-passive prosthesis with two-speed transmission.” Submitted to IEEE/ASME Transactions on Mechatronics.

[22] Finn-Henry, M., Baimyshev, A., and Goldfarb, M., 2020, “Feasibility Study of a Fall Prevention Cold Gas Thruster,” *8th IEEE RAS/EMBS International Conference for Biomedical Robotics and Biomechatronics (BioRob)*, pp. 611-616, doi: 10.1109/BioRob49111.2020.9224425.

CHAPTER 2

DESIGN AND PRELIMINARY ASSESSMENT OF LIGHTWEIGHT SWING-ASSIST KNEE PROSTHESIS

1. Abstract

This paper presents the design and control of a lightweight swing assist (SA) knee prosthesis. The SA knee relies on passive stability to provide support during the stance phase of walking and incorporates a small motor and battery to actively assist the knee motion during the swing phase. A prototype SA knee was constructed and experimentally evaluated on a single transfemoral amputee. The experiments consisted of treadmill walking at three speeds, first on a daily-use passive prosthesis and subsequently on the SA prosthesis prototype, while recording motion capture and ground reaction force data from which prosthesis knee kinematics and affected-side hip torque were computed. A comparison of the passive daily-use prosthesis and the SA prosthesis indicates that the SA prosthesis provides more consistent and repeatable knee motion and reduces pre-swing peak hip torque across all walking speeds.

2. Introduction

There are approximately 600,000 persons living in the US with major lower limb amputation, approximately half of whom have transfemoral amputation (TFA) [1]. The worldwide prevalence of TFA is approximately 20-30 times the US prevalence [2].

Multiple types of knee prostheses exist to help restore legged mobility to individuals with TFA [3]. The two primary functions of a knee prosthesis are to provide support (called stance control) during the stance phase of walking and to provide appropriate motion during the swing phase. Traditional passive prostheses typically provide stance phase stability via a hyperextension stop which is engaged by a combination of hip torque and ground reaction force. In some passive prostheses, knee stability during stance is further supplemented by the introduction of stance phase

damping, either engaged by microprocessor control (e.g., C-leg) or by mechanical sensing of stance phase (e.g., Mauch knee).

The essential aspects of swing phase are sufficient knee flexion to assure toe clearance (i.e., to avoid scuffing the ground during swing) and subsequent sufficient knee extension, which is necessary to achieve knee stability for the following stance phase. Passive knee prostheses achieve swing-phase motion by providing a low resistance which, when combined with the (active) swing phase movement of the residual thigh, in combination with the inertial properties of the lower leg, results in an initial swing-phase knee flexion, followed by knee extension. In some microprocessor-controlled knees (MPKs), swing knee resistance is modulated as a function of walking cadence. In all cases of passive prostheses (i.e., non-MPK and MPK), swing phase is resistive. Since knee extension at the swing completion is imperative, many passive knee prostheses employ an "extension aid" which is essentially a spring that helps promote full knee extension. Such an extension aid, however, opposes knee flexion and therefore promotes late-swing knee extension at the expense of limiting mid-swing knee flexion. In all passive prostheses, achieving proper swing-phase knee motion is an open-loop process – the user must provide the appropriate thigh motion to achieve a desired motion through the passive dynamics of the leg. As with all open-loop systems, the output of the system (in this case the motion of the knee) is sensitive to disturbances (e.g., scuffing or stumbling), and also sensitive to changes in the model, such as those that might occur as a result in changes footwear, ground slope, or environmental temperature. This lack of robustness is further exacerbated by the lack of proprioception at the prosthetic knee.

In order to address some of the deficiencies of passive prostheses, prostheses with powered joints (e.g., Power Knee) have been developed. The recent review [4] enumerates over 20 powered prosthesis prototypes (e.g., [5-7]). Powered knee prostheses typically utilize a motor and drive system to provide both stance-phase support and swing phase motion at the knee. In doing so, the swing phase motion can be driven to a specific trajectory, and therefore the swing-phase motion can be substantially more robust relative to passive prostheses. Furthermore, since the

physical behavior of powered prostheses is largely software-programmable, they are able to offer a wide range of biomechanical functionality and thus can better adapt their behavior to various activities and terrain relative to passive prostheses [8]. Despite these advantages, the requirements of substantial joint torque and power associated with stance-phase activities in particular generally result in larger, heavier, and noisier prostheses relative to passive counterparts.

This paper proposes a hybrid approach to providing stance and swing control in which stance control is provided strictly by passive means, but swing control utilizes a small motor for assistance. The approach is therefore called a Swing Assist (SA) knee. The motor is a form of "extension aid" in a passive knee; rather than providing strictly extension, however, the motor is able to aid both flexion in mid swing and extension in late swing. The SA prosthesis is intended to inject small amounts of power during the swing phase in order to guide the knee through a swing trajectory. Since the assistance is associated with low-torque and low-power movements, the motor, transmission, and battery can be small, lightweight, and quiet relative to a fully-powered knee prosthesis. This paper describes a device prototype intended to explore the potential efficacy of an SA prosthesis; describes the prosthesis controller; and describes experiments on a single individual with transfemoral amputation (ITFA) that compares swing-phase characteristics provided by the SA knee with those of a commercially-available MPK.

3. Methods

3.1. Mechanical Design

Prosthesis design was preceded by dynamic simulations of swing phase in order to assess the amount of torque and power required to modify the swing-phase trajectory of a typical passive prosthesis by a maximum of 15 deg while still ensuring full extension in late swing. These simulations resulted in a nominal torque requirement of 5 Nm and a nominal power requirement of 65 W. In order to satisfy these requirements, the SA knee prototype, shown in Fig. 2-1, employs a Maxon EC45 70 W brushless DC motor, chosen for its torque and power characteristics and high torque density. The motor

drives a slider-crank mechanism using a leadscrew assembly, resulting in a non-linear transmission ratio. The transmission has an average ratio of 15(±1):1 for a knee angle range between full extension and approximately 75 deg, and it can provide peak torques of approximately 7 Nm in this range. The full knee range of motion is 105 deg, and it contains a hyperextension stop at full extension. The proximal end of the knee interfaces with a socket via a standard pyramid connector, which also allows appropriate stance-phase alignment. The distal end interfaces with a standard pylon via a split clamp machined into the prosthesis. Due to choice of a power screw with a large lead, the knee is highly backdrivable, and the reflected inertia of the motor rotor was calculated to be less than 5% of the shank rotational inertia about the knee joint.

The SA prototype is equipped with a battery and embedded electronics for self-contained operation. Sensing on the SA knee includes an absolute encoder at the knee joint, an incremental encoder at the motor, and an inertial measurement unit (IMU) on the embedded control board, which is affixed to the shank of the leg. All high and low-level control runs on the embedded system, which is powered by a 5-cell 18V LiPo battery, enabling untethered operation. The complete prosthesis mass, as shown in Fig. 2-1, including the embedded system and battery, is 1.07 kg. Note that this mass is comparable to other passive prostheses. Note also that the mass does not include the pylon shank or ankle/foot prosthesis used in the experiments subsequently described.

Figure 2-1. Swing-assist knee prosthesis prototype (shown without embedded system or battery).

3.2. Controller

The SA knee walking controller consists of three states: 1) Swing Complete (SC); 2) Pre-Swing (PS); and 3) Swing Active (SA). Note that the SC state nominally corresponds to early and middle stance; the PS state corresponds to late stance; and the SA state corresponds to swing phase. The controller cycles through these states during normal walking as indicated in the state machine in Fig. 2-2. The state controller moves between states based on the combination of IMU and knee angle measurements enumerated in Table 2-1. The controller begins in the SC state, where the motor is used to emulate the high damping of a typical passive prosthesis. Although the maximum torque provided by the motor is insufficient to prevent knee buckling without relying on the hyperextension stop, the existence of high damping in stance helps maintain the knee at the extension stop, thus providing some measure of added stability in stance.

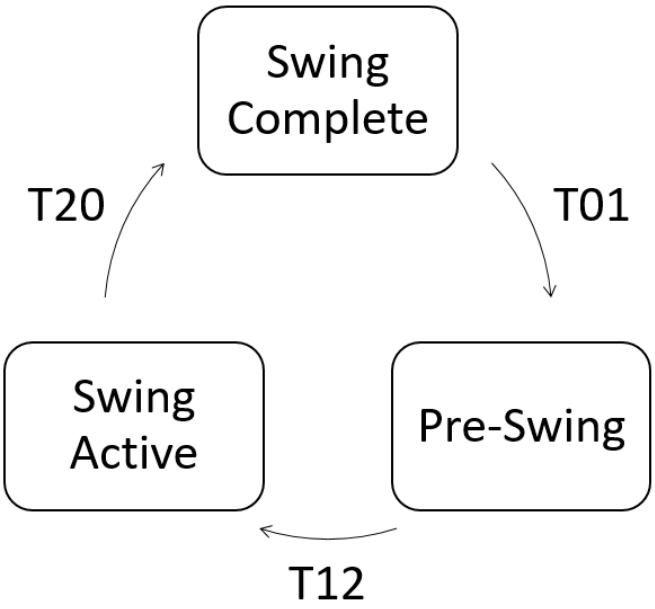

Figure 2-2. State flow chart.

The PS state is detected when the ITFA initiates swing phase with his or her residual thigh. As indicated in Table 2-1, this movement is indicated by a combination of shank angle, angular velocity, and linear acceleration along the shank. In this state the knee behavior remains passive (i.e., motor-emulated damping), although the damping is reduced to a lower value to enable the ITFA to initiate swing more easily.

Table 2-1. Walking controller state transitions.

Transition	Description	Condition
T01	Swing initiation.	Shank axial accel > 0.35 deg/s2 Shank angular velocity < 0 deg/s Shank angle < -25 deg
T12	Approximate transition to swing.	Knee angle > 20 deg
T20	Knee fully extended.	The swing trajectory is finished

Once the knee reaches 20 deg of flexion, the controller enters the SA state. Upon entering the SA state, the controller generates a cubic spline based on reference points

extracted from the knee swing of an average healthy person, matching both the knee angle and angular velocity at the PS to SA transition, using the combined durations of the SC and PS states to scale the duration of the trajectory. This method is adapted from [9] and similar to methods also employed in [10]. Note that the peak amplitude of knee flexion remains constant across cadences. Trajectory following in the SA state is maintained by a full state feedback controller that minimizes the reference tracking error, using the control law:

$$\tau = k_p(\theta_k - \theta_{kd}) + k_v\dot{\theta}_k \,, \tag{1}$$

where τ is the knee torque, θ_k is the knee angle, θ_{kd} is the desired knee angle based on the spline-generated trajectory, and k_p [Nm/deg] and k_v [Nms/deg] are position and velocity controller gains. At the end of swing the knee damping is ramped up to avoid shock from the impact of the knee joint and the hyperextension stop. Once the trajectory is complete, the controller switches into the SC phase in preparation for stance.

3.3. Experiment

The SA knee prototype and controller were tested on a 59-year-old male ITFA with a body mass of 93 kg. The experiment included walking on an instrumented treadmill at three speeds using first his daily-use passive prosthesis and then the SA knee prosthesis, while motion capture data and ground reaction forces were recorded. These experiments and associated protocol were approved by Vanderbilt University Institutional Review Board. A photograph of the subject with the SA knee prosthesis prototype on the instrumented treadmill is shown in Fig. 2-3. A standard pylon and passive carbon-fiber foot prosthesis were used with both prostheses, and both were used with the same socket.

Kinematic data collection was performed using a 10-camera (T40) system (Vicon) which was integrated with force plate measurements from the instrumented treadmill (Bertec FIT) via Vicon Nexus 2.5 software. A custom 42-marker skeleton was used to capture lower body and trunk motion. The motion capture marker data post-

processing was performed in Vicon Nexus 2.5 and then exported to MATLAB for stride parsing and alignment.

In the experiments, the subject first conducted walking trials at each of three speeds with his daily-use knee prosthesis (an Ossur Rheo Knee). The three speeds were based on his self-selected speed (0.9 m/s), and 20% slower and faster respectively (0.7 m/s and 1.1 m/s). The subject walked at a steady-state speed for 45 sec of data collection for each speed. Following data collection with the daily-use prosthesis, the subject was fit with the SA prosthesis prototype. After approximately 30 min of walking in parallel bars and overground with the prototype, the subject conducted the treadmill experiments with the SA prosthesis, at the same three treadmill speeds and with the same experimental protocol employed with the daily-use prosthesis.

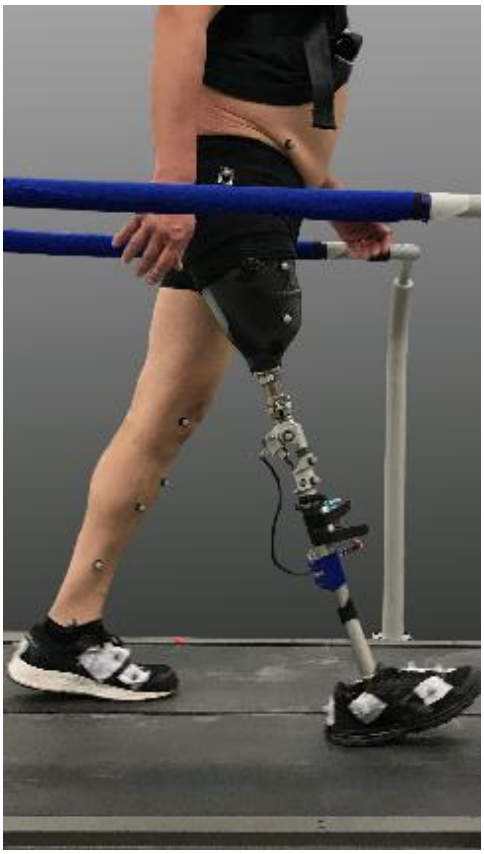

Figure 2-3. The transfemoral amputee test subject.

4. Results and Discussion

The assistive torque, averaged over 25 strides, applied by the SA knee motor when walking at normal speed (0.9 m/s) is shown in Fig. 2-4, along with the corresponding assistive power. The mean peak assistive torque and power are approximately 5.8 Nm and 28 W, respectively. Note that these torque and power requirements are substantially lower than typical powered prostheses, which are designed to provide knee torque and power an order of magnitude greater. Finally, it can be observed that the power is largely positive, thus indicating the assistive behavior of the SA prototype.

Fig. 2-5 shows the knee angle versus stride for each walking speed with the daily-use prosthesis in the left column, compared to those for the SA knee prosthesis in the right column. In the figure, each plot shows the mean of 25 strides, and also plus and minus one standard deviation about the mean. The data were parsed using heel strike, which was detected by ground reaction force measurement. To minimize the temporal misalignment among the strides, the data were also auto-correlated based on the knee angle. Table 2-2 summarizes the mean peak knee flexion angle for each prosthesis at each speed. As indicated in the table, the daily-use prosthesis resulted in peak knee flexion angles at the three walking speeds of 49.2, 55.0, and 60.7 deg, respectively, while the SA prosthesis resulted in peak knee flexion angles of 59.9, 61.1, and 61.4 deg respectively. In relative terms, the peak flexion angle of the daily-use prosthesis varies by plus/minus 10% when walking speed varies by plus/minus 20%, while the SA prosthesis peak knee flexion angle varies by only plus/minus 1% for the same speed variation. Fig. 2-6 shows the knee angle data collected across all three walking speeds; the difference in standard deviation provides another indication of the improved swing-phase uniformity offered by the SA prosthesis, relative to the daily-use.

Fig. 2-7 shows the affected-side hip moment for each prosthesis at each speed, averaged across the 25 strides at each speed. As seen in the figures, the SA prosthesis required significantly lower peak hip torques at the initiation of swing relative to the daily-use prosthesis. Table 2-3 summarizes the average peak hip moments for both

prostheses for each walking speed. For slow, normal, and fast walking, the SA knee required 23.7%, 27.1%, and 33.3% less peak hip torque, respectively, at swing initiation. The step-to-step variation in peak hip torque was determined to be normally distributed for each knee and walking speed, as tested by the Kolmogorov-Smirnov test, and differences in peak torques at each speed shown to be significantly different with p-value < 0.01. The authors recognize that the inertial properties of the two legs are not identical, and therefore some of this difference may be attributable to inertial differences. Thus, while promising, additional experiments will be required to validate the prospective reduction in hip torque required for swing.

Table 2-2. Peak Knee Flexion.

	Slow		Normal		Fast	
	Mean (deg)	Standard deviation (deg)	Mean (deg)	Standard deviation (deg)	Mean (deg)	Standard deviation (deg)
Passive	49.2	2.2	55.0	1.8	60.7	1.3
SA knee	59.9	1.0	61.1	1.3	61.4	0.7

Table 2-3. Peak Hip Moments.

	Slow (Nm)	Normal (Nm)	Fast (Nm)
Passive	62.3	83.3	99.7
SA knee	47.5	60.7	66.5

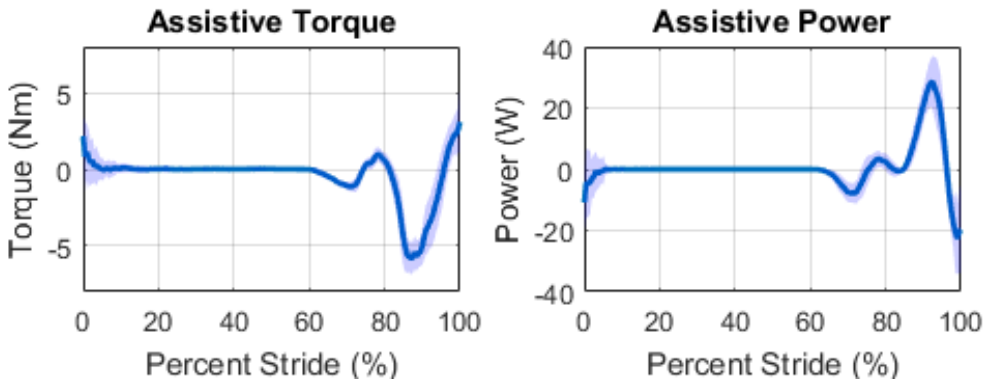

Figure 2-4. Assistive knee torque (left) and power (right) applied by the motor. Solid line is the mean, while the band indicates plus/minus one standard deviation.

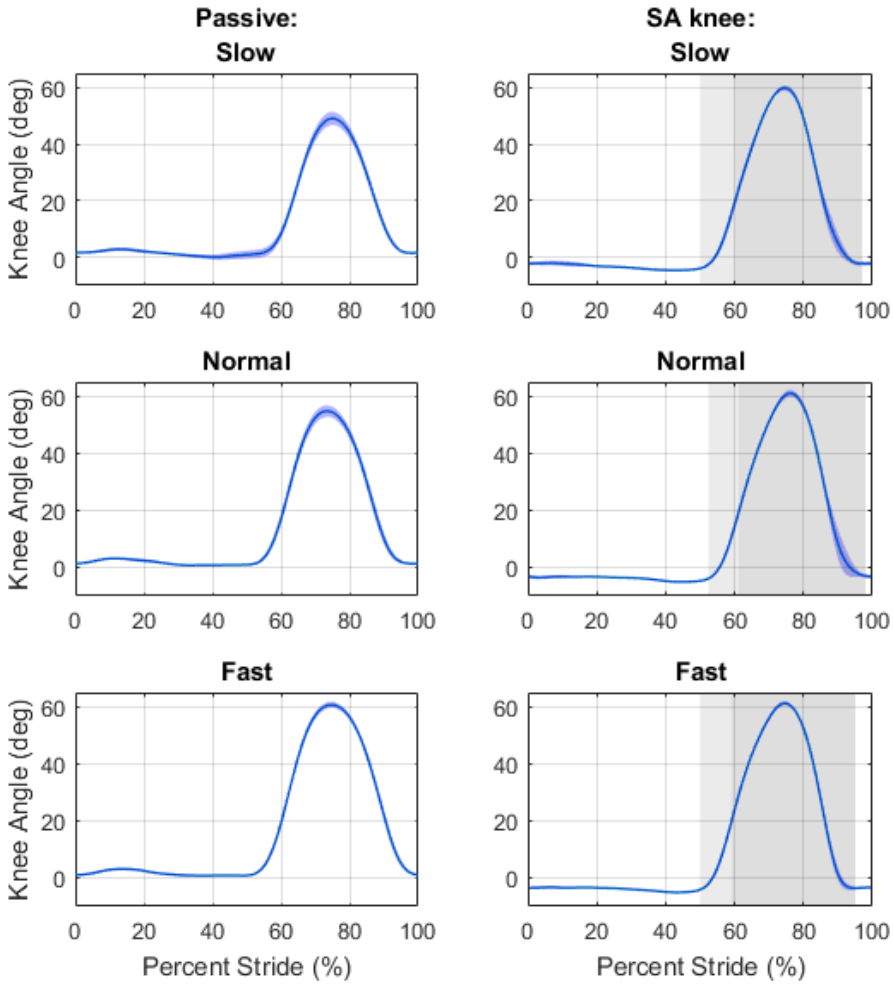

Figure 2-5. Comparison of passive and SA prosthesis knee angles across different speeds. Solid line is the mean, while the light band indicates plus/minus one standard deviation about the mean. White background indicates Swing-Complete, light gray indicates Pre-Swing, while dark gray indicates Swing-Active states.

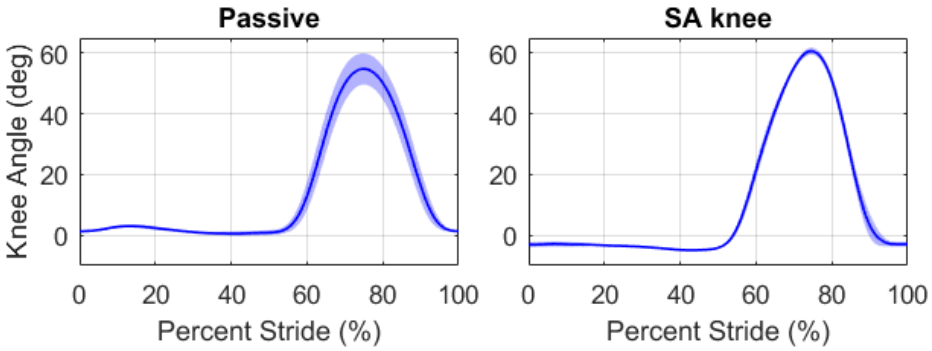

Figure 2-6. Comparison of passive and SA prosthesis knee angles across all speeds. Solid line is the mean, while the band indicates plus/minus one standard deviation.

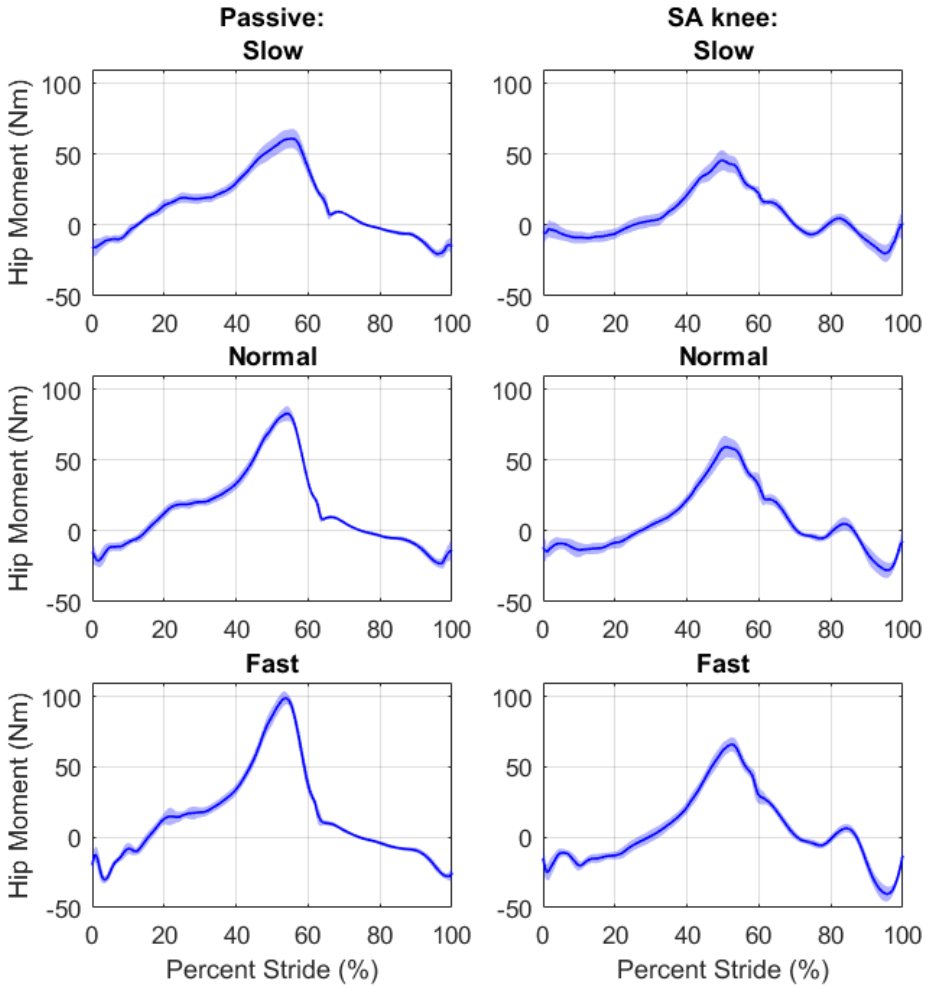

Figure 2-7. Affected side hip moments for passive and SA knees. Solid line is the mean, while the band indicates plus/minus one standard deviation.

5. Conclusion

The addition of swing assist in the SA knee appears to offer a more repeatable and consistent swing-phase motion across walking speeds compared to a daily-use passive prosthesis, while maintaining a similar size, weight, and low-noise operation. Further, preliminary data indicate that the SA prosthesis provides a substantial reduction in peak hip torque required to initiate swing. These results indicate promise with respect to providing greater consistency to ITFA during swing phase. Future work will include expanding the experimental protocol and number of subjects to more thoroughly investigate these results.

6. References

[1] K. Ziegler-Graham, E. MacKenzie, P. Ephraim, T. Travison and R. Brookmeyer, "Estimating the Prevalence of Limb Loss in the United States: 2005 to 2050", *Arch Phys Med Rehabil*, vol. 89, no. 3, pp. 422-429, 2008.

[2] R. Renzi, N. Unwin, R. Jubelirer and L. Haag, "An International Comparison of Lower Extremity Amputation Rates", *Annals of Vascular Surgery*, vol. 20, no. 3, pp. 346-350, 2006.

[3] Romo, H.D. "Prosthetic knees." *Phys Med Rehabil Clin N Am*, vol. 11, no. 3, pp. 595–607, 2000

[4] M. Windrich, M. Grimmer, O. Christ, S. Rinderknecht and P. Beckerle, "Active lower limb prosthetics: a systematic review of design issues and solutions", *BioMedical Engineering OnLine*, vol. 15, no. 3, 2016.

[5] F. Sup, A. Bohara and M. Goldfarb, "Design and Control of a Powered Transfemoral Prosthesis", *The International Journal of Robotics Research*, vol. 27, no. 2, pp. 263-273, 2008.

[6] B. Lambrecht and H. Kazerooni, "Design of a semi-active knee prosthesis", *2009 IEEE International Conference on Robotics and Automation*, 2009.

[7] E. Rouse, L. Mooney and H. Herr, "Clutchable series-elastic actuator: Implications for prosthetic knee design", *The International Journal of Robotics Research*, vol. 33, no. 13, pp. 1611-1625, 2014.

[8] M. Goldfarb, B. Lawson and A. Shultz, "Realizing the Promise of Robotic Leg Prostheses", *Science Translational Medicine*, vol. 5, no. 210, pp. 210ps15-210ps15, 2013.

[9] B. Lawson, J. Mitchell, D. Truex, A. Shultz, E. Ledoux and M. Goldfarb, "A Robotic Leg Prosthesis: Design, Control, and Implementation", *IEEE Robotics & Automation Magazine*, vol. 21, no. 4, pp. 70-81, 2014.

[10] T. Lenzi, L. Hargrove and J. Sensinger, "Minimum jerk swing control allows variable cadence in powered transfemoral prostheses", *2014 36th Annual International Conference of the IEEE Engineering in Medicine and Biology Society*, 2014.

CHAPTER 3

FEASIBILITY OF A WEARABLE COLD-GAS THRUSTER FOR FALL PREVENTION

1. Abstract

This paper examines the feasibility and control authority of an electronically-controlled cold-gas thruster (CGT) as a backpack-worn device for fall prevention for individuals at fall risk. The CGT is comprised of a pressurized air tank combined with a custom electrically actuated high-flow-capacity valve and servo-controlled nozzle, which are employed together to create a thrust intended to arrest an impending fall. In this paper, the authors present the design of the CGT prototype and experimentally investigate its prospective control authority for purposes of correcting an impending fall. In order to experimentally assess the extent to which the prototype provides sufficient control authority necessary to restore balance from a state of imbalance, the prototype was attached to an approximately human-scale rocking block (i.e., a block with similar mass, inertia, and basin of stability characteristics to a standing human). Experiments were conducted that measured the ability of the CGT prototype to return the block back to its basin of stability, when configured in an initial configuration outside of it. For a block with a nominal (passive) basin of stability defined by a 7.6 deg tilt angle relative to the vertical, the CGT prototype was able to restore the block back to its basin of stability for tilt angles up to 25 deg, indicating a promising amount of control authority for the purpose of restoring balance to individuals at fall risk.

2. Introduction

Falls can lead to severe and fatal injuries, particularly for elderly people, and fear of falling can lead to loss of independence [1]. According to the U.S. Centers for Disease Control and Prevention, one in four people over the age of 65 fall every year. In 2014, approximately 2.8 million fall-related injuries were reported by older adults in the US. Of these, 27,000 were fatal, while others resulted in injuries ranging from minor lesions and bruises to life-threatening hip fractures and traumatic brain injuries [2]. Balance

ability declines with age due to several physiological changes: the performance of the musculoskeletal system deteriorates both in strength and speed, and sensory systems, including visual, vestibular, and proprioceptive, incur increased reaction time [3]. In order to address the risks associated with falls, several fall prevention solutions are available for use in home environments, including handrails, high friction flooring, and improved lighting. Most falls, however, occur outside the controlled home space; few fall prevention devices exist for use outside the home, and as such, portable fall-prevention approaches for unstructured environments are needed [4].

Wearable devices offer a possible fall mitigating intervention that does not rely on a structured environment. Robotic exoskeletons can potentially offer balance assistance in a wearable manner. A recently published review describes various proposed methods for providing balance assistance with lower limb exoskeletal devices [5]. Among the related efforts are those described by [6-14]. Although these approaches have promise for balance assistance, none have yet been described for the purpose of recovery from an impending fall, such as the intent of the approach proposed here. Since exoskeletons generally provide a floor-referenced force, they are more constrained (relative to the approach described here) in providing forces to the torso relative to an inertial reference frame (IRF), and therefore the issue of correcting an impending fall becomes more challenging. Also, the need to coordinate actions between the user and device at the limb level likely increases the complexity of the control challenge, and a mismatch between limb-level reaction strategy between the device and user could potentially obstruct the user's efforts at recovery.

Rather than provide fall correction via the assistance of limb motion, an alternative approach is to exert an external force or moment directly to the human body (e.g., torso) with respect to the IRF. This approach removes the aforementioned limitations of floor-reference forces, and also lessens the need to coordinate precisely with the user's recovery strategy, thus reducing the complexity of the control problem and mechanical structure of the device. Recently, researchers have employed this approach via the use of control moment gyroscopes (CMGs) in a backpack form to impose controllable torques directly to a user's trunk [15-19]. A recent study with

human participants demonstrated improvements in balance while standing and walking using a CMG controlled to emulate a damping field in the IRF [20]. Although shown to be an effective solution for balance assistance, a CMG may be less able to arrest an impending fall, since the design of a lightweight device limits the magnitude of moment and moment impulse. Specifically, there is a design trade-off between the size of the device, the rotational speed and mass of the flywheel(s), and the magnitude of the resulting moment and moment impulse, which together requires a compromise between size, weight, vibration, audible noise, quiescent power consumption, and magnitude of the achievable control moment impulse.

Another way of applying an external force to the user's body with respect to an IRF is via a thruster, which appears not to have yet received attention in the literature for this application. A cold-gas thruster (CGT) typically employs a compressed gas, such as nitrogen or carbon dioxide, which flows through a nozzle to produce a force relative to the IRF via the rate of change of momentum of the gas. The characteristics of the generated force are influenced primarily by gas pressure, volume, molecular weight, and nozzle characteristics. Since the fundamental source of momentum is a gas that can be compressed to a small volume at low weight, a CGT may have appropriate characteristics as a lightweight portable emergency fall prevention measure. In addition, a CGT would require no significant idle power and entail no quiescent noise (i.e., it will generate noise only when thrusting).

The objective of this paper is to investigate the feasibility of a CGT-based fall prevention device, envisioned as a backpack-worn device (as shown in Fig. 3-1), to prevent an impending fall once it has already begun. The device is intended to perform the same function a caregiver would provide when an individual at fall risk loses balance; namely, to provide a corrective force to effectively "catch" the person falling, and subsequently allow them to recover a stable posture. In this paper, the authors describe the design of a novel CGT device capable of an appropriate corrective force impulse; present the design of a lightweight, high-flow, high-pressure, fast-acting pneumatic valve necessary to realize the CGT; present a controller, based on a simplified model of a backward-falling person, intended to provide an appropriate corrective

impulse for the control authority experiments presented herein; and present the results of experiments intended to assess the control authority of the CGT for purposes of potentially preventing falls.

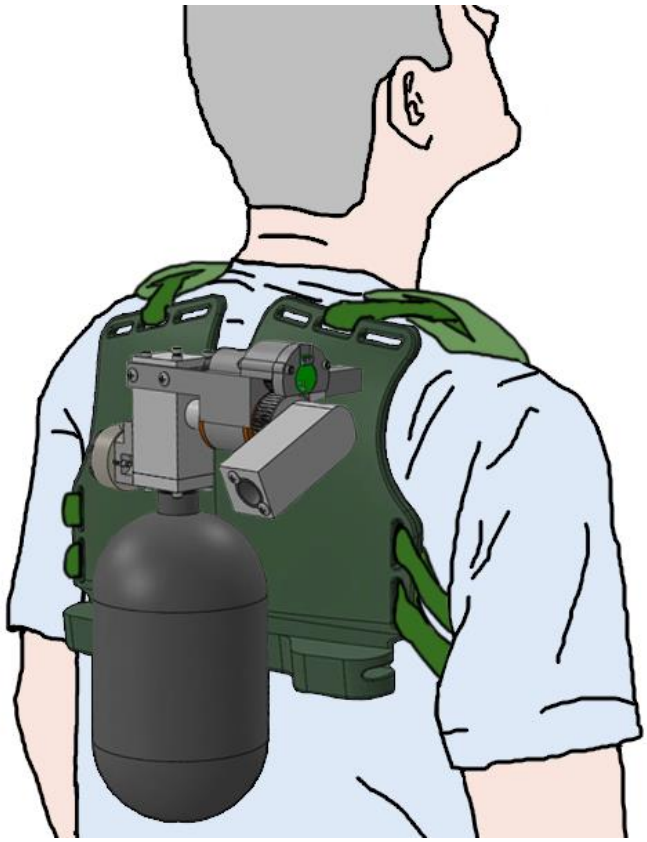

Figure 3-1. Concept drawing of backpack-worn CGT for correction of impending fall.

3. CGT Design Specifications

The proposed CGT approach (as illustrated in Fig. 3-1) is only feasible if it is able to provide an inertially-referenced force and force impulse of a magnitude sufficient to substantially correct an impending fall. In order to explore the feasibility of such a device, the authors initially consider correcting backward falls during standing. This section discusses and justifies the consideration of backward fall prevention during standing and describes how the authors estimate the force magnitude and impulse sufficient to substantially correct impending backward falls. If a CGT can be successfully

implemented to provide the characteristics associated with this functionality, it can presumably be expanded in future work to include broader functionality.

3.1. Standing Balance

A standing person can be considered in stable balance if their center of pressure (COP), which is the vertical projection of their center of mass (COM) onto the ground, lies within their base of support (BOS), roughly defined as the polygon that envelops the contact area between their feet and the ground. The BOS boundaries are often referred to in standing balance as the limits of stability (LOS) [21]. As the COP approaches the LOS, a person typically responds by performing compensatory trunk and arm motions to bring the COP within the LOS. In cases when the COP moves outside the LOS, a common response involves a step in the direction of the fall, which alters the shape of the BOS to encompass the COP. This strategy is called change-in-support (CIS) action [22]. A scenario when a CIS action fails will result in a fall. The severity of the fall and consequent damage depends on the direction of the fall, impact velocity, and impact location on the body. Some directions of fall offer more opportunities to reduce the impact velocity than others. A person falling forward has the greatest visual feedback and can use their knees and hands to decelerate the fall. Lateral falls offer partial visual feedback and can be decelerated using hands and elbows. Backward falls offer little to no visual feedback and limited ability to use hands [23].

In elderly individuals, the LOS is reduced in all directions [24], which requires quicker and more frequent use of the CIS strategy. However, a slower response time and weakened musculoskeletal system diminishes the efficacy of the CIS strategy, relative to a younger population [22]. Fall mitigation techniques are also less accessible to the elderly since they require greater levels of agility and strength and may still result in injuries. Mobility aids, such as walkers and canes, increase the stability of their users by expanding their base of support forward and sideways, although the LOS in the backward direction remains largely unchanged.

This paper explores the prospective utility of a CGT to provide corrective assistance for backward falls. In the case of backward falls: 1) LOS is the smallest; 2)

visual feedback is most limited; 3) mitigation techniques are least effective; and 4) existing assistive devices (e.g., a rolling walker) have limited utility. Therefore, for purposes of this paper, the primary design objective of the device is to effectively expand the backward LOS, which would reduce the need for a user to resort to a CIS strategy. In the case when the COP exits the expanded LOS, a secondary objective of such a device would be to reduce the fall velocity by slowing the fall, therefore increasing the time window for a CIS action. Therefore, for the purposes of this feasibility study, this paper considers only the objective of expanding the backward LOS.

3.2. Backwards Fall Experiments

Among the primary feasibility issues in the design of a CGT is the extent to which a small, lightweight device (i.e., suitable as a backpack-worn device for individuals at fall risk) is capable of providing an inertially-referenced corrective force and impulse of suitable magnitude to arrest or correct an impending fall. The authors were unable to find prior studies that characterize these requirements. As such, a simple experiment was conducted to provide an estimate of corrective forces required to arrest an impending backward fall. The experiment is illustrated in Fig. 3-2(a), with a conceptual equivalent with a CGT shown in Fig. 3-2(b). In the experiment, subjects wore an upper-body harness with a rope affixed to the chest of the harness, which was instrumented with a load cell (Transducer Techniques MLP-500) to measure tensile forces in the rope. During the experiment, subjects voluntarily fell backward, keeping their body in an approximately straight posture. At a body angle of approximately 15-20 deg, the fall was arrested by a separate individual, who pulled the rope and restored the subject's standing balance. In addition to forces in the rope, the experiment was recorded by a motion capture system (Vicon, Oxford GBR), with motion capture markers attached to both ends of the rope to measure the angle of the applied force, and to the subject's left shoulder, left hip, and to the floor next to the subject's heels, to measure the subject's nominal body orientation. The experiment was repeated five times for each subject and repeated for three subjects (males of body mass 54 kg, 72 kg, and 80 kg, respectively),

in order to provide an estimate of the force associated with correcting a potential backward fall and to confirm that such corrective forces would not injure the user.

Figure 3-3 shows the measured component of the average force imparted by the rope orthogonal to the body (in blue), and the corresponding average angle between the subject's vertical axis and the ground normal (in red), adjusted such that the equilibrium angle is zero. The bold lines represent the mean across all trials, while the shading represents plus and minus one standard deviation from the mean. Note that positive angles are in the backwards direction as shown in Fig. 3-2(a). These experiments indicate that, for the range of body masses tested between 54 and 80 kg, fall recovery from an angle between 14 and 22 deg requires corrective forces with a peak magnitude between 300 and 500 N and total duration of approximately 0.7 s. According to subjective feedback, fall correction did not induce discomfort or pain during the experiments.

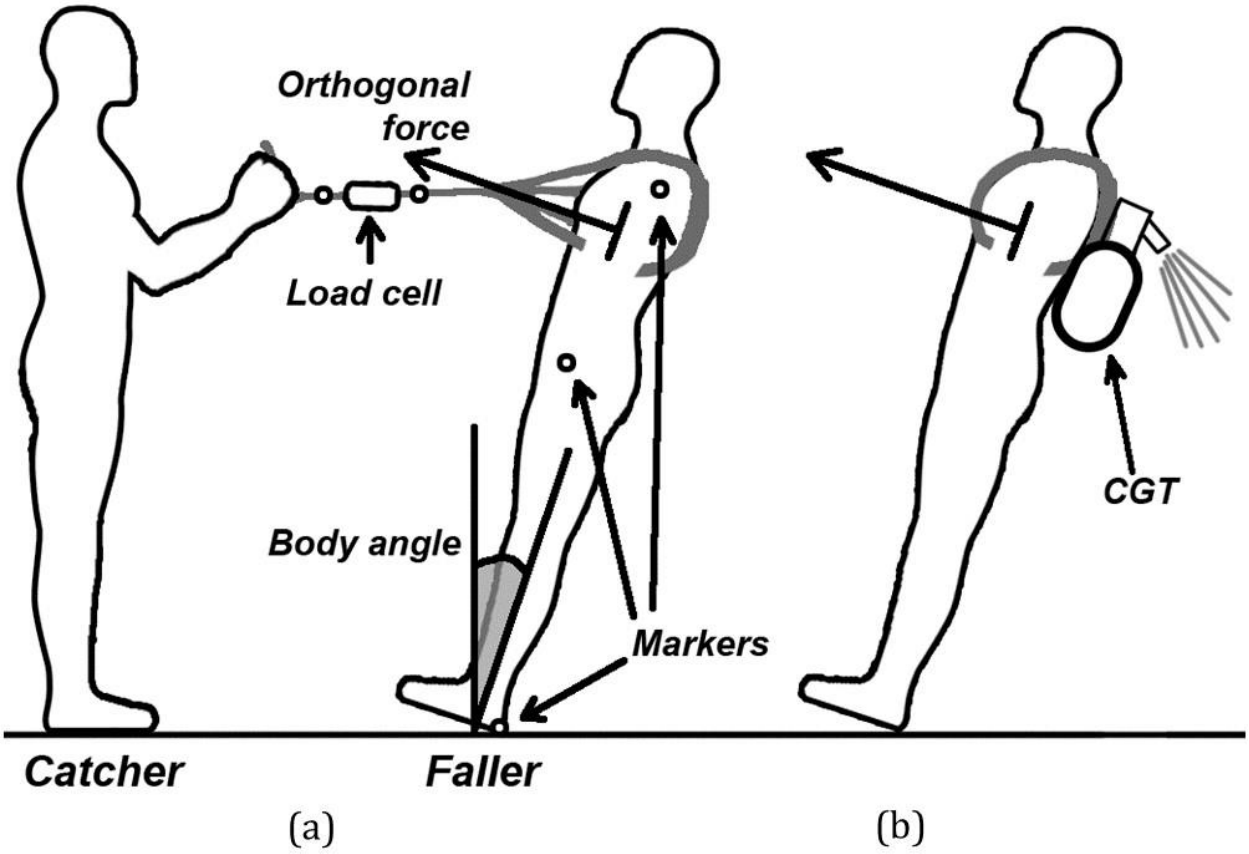

Figure 3-2. Backward fall experiment to estimate corrective force characteristics required to correct an impending fall: (a) experimental diagram and (b) conceptual CGT-based equivalent force.

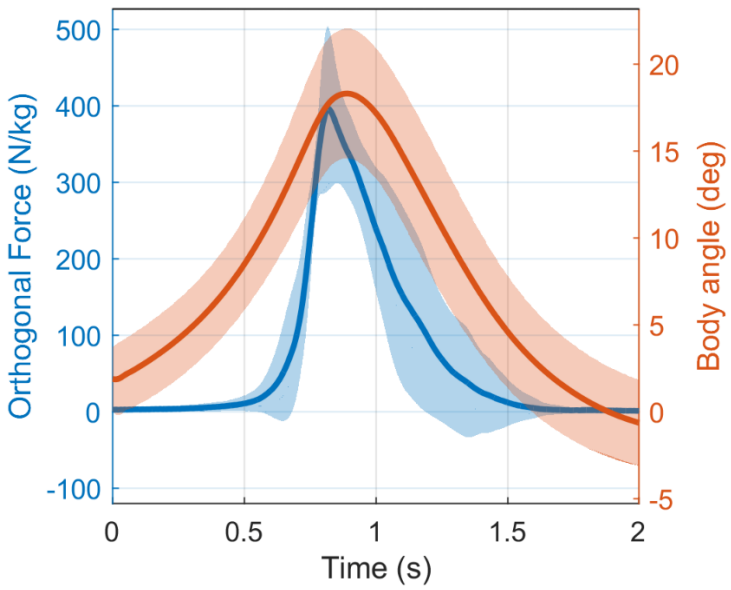

Figure 3-3. Orthogonal rope tension (left axis, blue), body angle (right axis, red).

4. CGT Design

A CGT prototype was designed with the objective of providing the desired nominal force profile shown in Fig. 3-3. The prototype, shown in a solid model in Fig. 3-4, is comprised of three essential subsystems: 1) a gas thruster; 2) a high-throughput fast-acting valve; and 3) a single-axis servo system that controls the orientation of the nozzle in the thrust plane. The axis of rotation of the nozzle servo system is also shown in Fig. 3-4. Figure 3-5 shows a cross-section of the prototype and the path of the cold gas flow from the compressed gas tank, through a solenoid-actuated valve (shown with valve open in the figure), and then out through the nozzle to create the restorative thrust force. The design of each subsystem is discussed in the following subsections. The assembled CGT prototype has a total mass of 2 kg, with dimensions occupying a volumetric envelope of 30 cm x 18 cm x 11 cm. The approximate scale of the system, and the manner in which it would be worn by a user, are illustrated in Fig. 3-1.

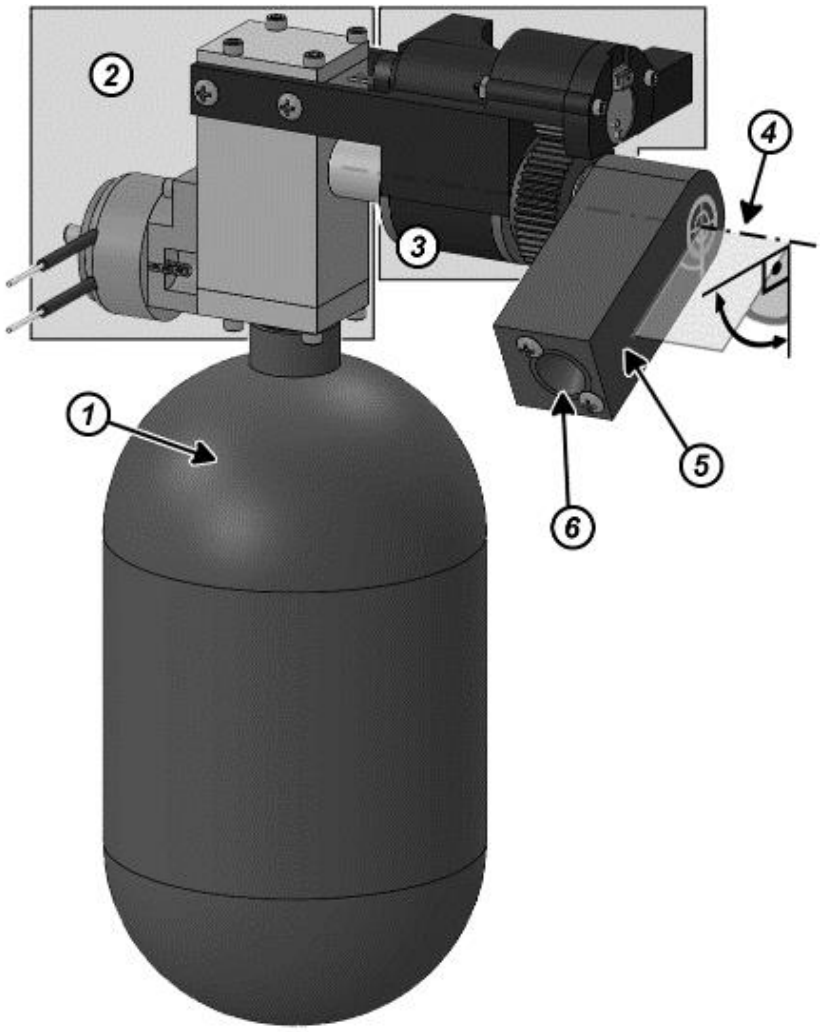

Figure 3-4. CGT prototype. The labels identify: (1) compressed gas tank; (2) valve subsystem; (3) nozzle servo subsystem; (4) nozzle servo axis; (5) nozzle housing; and (6) nozzle exit.

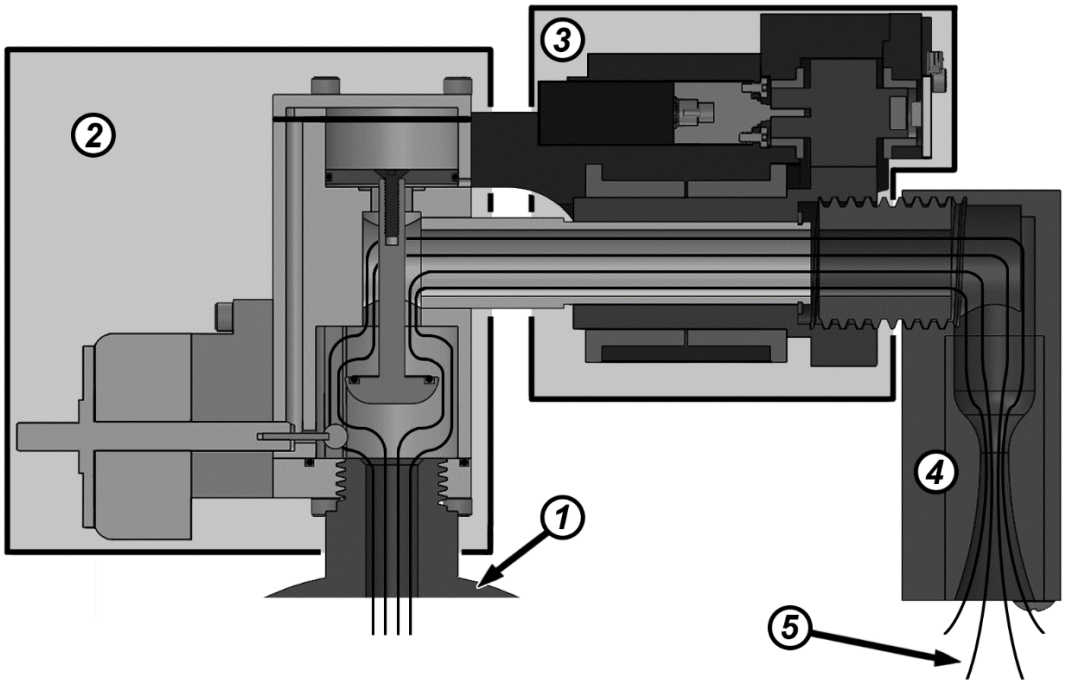

Figure 3-5. Cross-section of CGT. Streamlines (5) show the gas flow path during force generation, where gas flows from the tank (1), through the valve subsystem (2), then through the servo subsystem (3), and finally through the nozzle (4).

4.1. Gas Thruster Subsystem Design

The cold-gas thruster subsystem consists of the compressed gas tank and converging-diverging nozzle shown in Fig. 3-5. These two elements comprise a single design component (i.e., the thruster), although they are physically separated by the high-throughput control valve and servo-control subsystems situated between the two. The valve and servo-control are separate subsystems, and are discussed in subsequent subsections. For the purposes of thruster design, only the compressed gas tank and nozzle are considered in this subsection. For the CGT, standard nozzle design equations were employed [25-27] (see Addendum), assuming an ideal gas undergoing isentropic flow. The major design parameters that determine the characteristics of thrust produced by the thruster include: 1) the species of gas; 2) tank volume and initial pressure; and 3) the nozzle throat (narrowest point) and exit diameters. Nitrogen was selected as the gas species, since it has a high molecular weight (increases thrust), is non-toxic, and low cost [28]. A tank volume of 1 L was determined to be viable for a

backpack-worn device; as such, a 1 L carbon-fiber tank rated to a maximum pressure of 31 MPa (4500 psi) was selected (Ninja Paintball, Crystal Lake IL). Despite the potential to charge the tank to a pressure of 31 MPa, the authors selected 10 MPa (1500 psi) instead for the work presented here, to provide an added factor of safety for the prototype design. Given these parameters, the nozzle throat and exit diameters were selected as 5.4 mm and 15.4 mm, respectively (resulting an exit area to throat area ratio of 8.13 and an exit Mach number of 3.7), to provide thrust duration similar to the one measured in the backwards fall experiments shown in Fig. 3-3. The nozzle was fabricated using additive manufacturing methods from ABS resin, with converging and diverging half-angles of 30 deg and 10 deg respectively, which correspond to commonly used nozzle design practices for balancing nozzle length and losses [29]. A summary of thruster design parameters is given in Table 3-1. For purposes of the subsequent control law design, the resulting thrust over time produced by these design parameters is approximated by:

$$F(t) = F_{max} e^{-t/\tau}, \tag{1}$$

where F_{max} is 370 N and τ is 0.14 s. Note that the expected peak force is roughly equal to the average peak force of 400 N observed in the fall experiments shown in Fig. 3-3. Note that the thrust magnitude can be tripled (i.e., 1100 N) if desired or required in a subsequent prototype by increasing the tank pressure to the rating of the tank.

Table 3-1. CGT Parameters

Name	Value	Description
γ_{N2}	1.4	Nitrogen heat capacity ratio
R_{N2}	296.8 J/[kg*K]	Nitrogen specific gas constant
P_0	1.034e+7 Pa	Tank pressure
V_0	1.11e-3 m^3	Tank volume
T_0	298 K	Tank temperature
m_0	0.13 kg	Mass of N_2 in the tank
d_t	5.4 mm	Nozzle throat diameter
d_e	15.4 mm	Nozzle exit diameter

4.2. Gas Valve Subsystem Design

A custom high-throughput, fast-acting solenoid valve, shown in solid-model in Fig. 3-6, was designed to activate the CGT in the event of an impending fall. The valve is situated between the tank and nozzle, at the tank exit, as shown in Fig. 3-5. The valve requires a minimum orifice area larger than the nozzle throat (i.e., to avoid a substantial pressure drop across it during the thrust event); must open in a time much shorter than the characteristic time associated with a fall (i.e., so that the thrust occurs near the onset of the impending fall); must be able to operate at the rated pressure of the system; and must be of a positive-sealing type, since it is must effectively seal the gas within the compressed gas tank when the CGT is not in use.

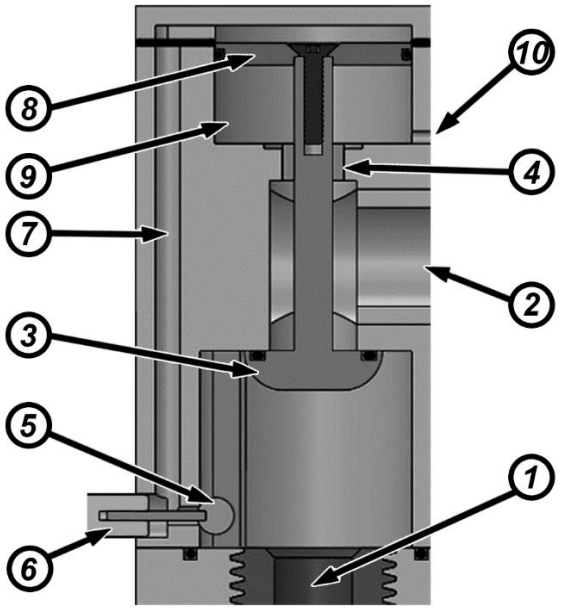

Figure 3-6. Cross-section of high-throughput fast-acting pilot-operated poppet valve, showing: (1) valve inlet; (2) valve outlet; (3) main poppet; (4) main poppet bearing; (5) pilot poppet; (6) solenoid rod/core; (7) pilot flow channel; (8) pilot piston; (9) pilot cylinder; and (10) pilot vent.

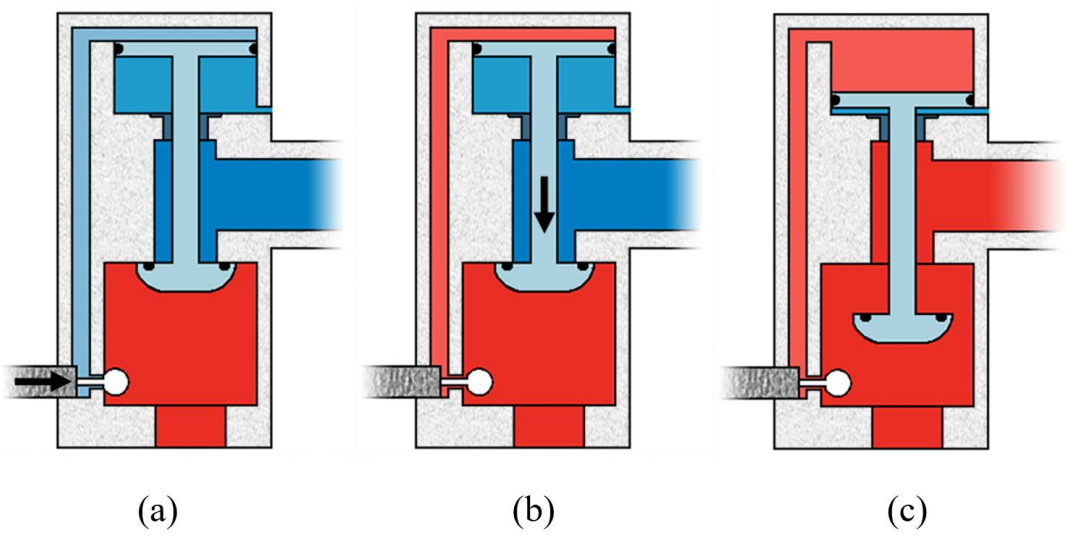

Figure 3-7. Schematic illustration of solenoid-actuated, pilot-operated, high-throughput, fast-acting poppet valve, showing: (a) valve closed; (b) pilot open; and (c) valve open.

Based on standard gas flow equations, for a given volumetric flow, the pressure drop across each component in the system will be approximately proportional to the minimum cross-sectional area of that component. Therefore, in order to maximize the thrust generated for a given tank pressure, the minimum cross-sectional area in the valve should be much greater than the throat area of the nozzle (23 mm^2 for the specified nozzle throat diameter of 5.4 mm). For a valve flow area of roughly 100 mm^2 (i.e., 4 times the nozzle throat) at a pressure of 10 MPa, the force associated with blocking the valve orifice would be 1000 N (224 lb). A force of this magnitude is incompatible with a low-weight electromechanical actuator, particularly if fast activation is required. Note that such pressure-based actuation forces can be reduced by implementing pressure-balanced valve design, such as a spool-type valve; such designs, however, are susceptible to leakage and not generally suited to positive-sealing designs. As previously stated, the valve in this system should be a positive-sealing type valve, since it should effectively seal the nitrogen gas in the tank for days or weeks without noticeable loss. Therefore, the authors choose to implement a pilot-operated poppet-type valve design, which is well-suited to positive sealing, enables a fast-acting response, and enables a high-throughput gas flow (i.e., can be designed to accommodate a large valve throat area).

A cross-section of the CGT valve, depicted in the closed (i.e., sealed) position, is shown in Fig. 3-6. In the closed position, high-pressure gas (i.e., 10 MPa) pressurizes the valve inlet. In order to open the valve, a solenoid actuator (Testco Ledex 129440-028) is energized, which opens the pilot poppet. The pilot poppet covers an orifice that is 2.4 mm in diameter, which at 10 MPa, requires a force of 45 N (10 lb) from the solenoid. When the pilot poppet is opened, high-pressure gas flows through the pilot flow channel into the pilot cylinder, which pushes the pilot piston downward to open the main poppet. When the main poppet opens, the valve orifice area (i.e., the annular area around the main poppet) is approximately 106 mm^2. Based on subsequently described experiments validating thrust, the valve response time (from solenoid command to pressurized outlet) is approximately 30 ms. The operation of the valve is schematically illustrated in Fig. 3-7, which shows the valve in the initial resting state of the valve in Fig. 3-7(a), where red indicates high-pressure regions and blue indicates low-pressure regions; immediately following energizing the solenoid in Fig. 3-7(b), where the high-pressure gas flows into the pilot cylinder; and in its fully open state in Fig. 3-7(c), where the main poppet is fully-open and gas can flow through the valve. For the prototype described here, the valve body was machined from 7075 aluminum alloy, and poppet from 303 stainless steel.

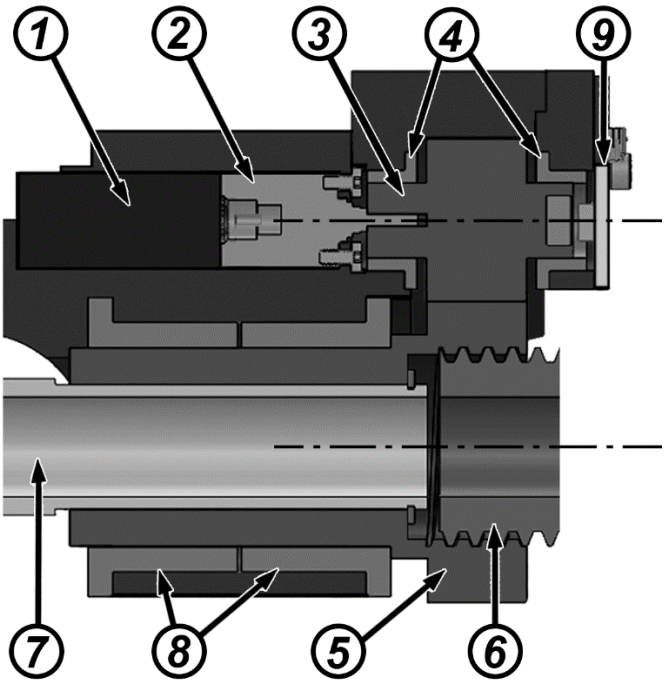

Figure 3-8. Cross-section of servo subsystem, showing: (1) brushless DC motor; (2) planetary gearhead; (3) pinion; (4) pinion bearings; (5) output gear; (6) nozzle housing; (7) valve outlet tube; (8) output gear bearings; and (9) absolute encoder.

4.3. Nozzle Servo Subsystem Design

The CGT employs a servo system that controls the angle of the nozzle (and therefore the thrust vector) about the axis of rotation as shown in Fig. 3-4. The main components of the nozzle servo subsystem are depicted in Fig. 3-8. The servo system is actuated via a brushless DC motor (Faulhaber 1226A012B) which drives a pinion spur gear through a 64:1 planetary gearhead. The pinion drives an output gear, which rotates on the valve outlet tube. The nozzle is affixed to the output gear, and therefore rotates with it. Note that the servosystem must allow rotation of the nozzle, but also prevent leakage of the high-pressure gas. As such, the nozzle housing is threaded into the main gear, and the main gear shaft rotates on the valve outlet tube with a close sliding fit, to prevent gas leakage during the thrust event (recall that the pressure remains high in this section, since the primary pressure drop is downstream across the nozzle throat). An absolute encoder (Austria Microsystems AS5145) is mounted between the pinion and

housing to provide angle information for servo feedback control. The servo subsystem can rotate the nozzle through a range of motion of approximately 180 deg.

4.4. Design Considerations for Safety

Note that the CGT prototype was designed for purposes of assessing control authority with respect to correcting an impending fall. Nonetheless, since the CGT employs pressurized gas, and is eventually intended as a backpack-worn device, the design should reflect appropriate design factors of safety. The system can be viewed as two subsystems: one that contains the high-pressure compressed gas over long periods of time, and another that is exposed to high pressure gas flow only occasionally for short durations. Specifically, the tank and inlet side of the poppet valve are exposed to 10 MPa (1500 psi) continuously, while the outlet side of the valve and nozzle are exposed only for a brief (approximately 0.7 s) pressure transient (i.e., see pressure profile in Fig. 3-10). The 1 L carbon-fiber tank is rated from the manufacturer to a working pressure of 31 MPa (4500 psi); this tank is designed by the manufacturer according to ASME standards, which requires a factor of safety of 3.5. Since the pressure vessel is used here at a working pressure of 10 MPa (i.e., 1/3 of the working pressure), the tank has a design factor of safety of over 10 for this application. The valve inlet for the CGT prototype was designed by the authors also with a minimum factor of safety of 10. Therefore, the components that are exposed to continuous pressure are both being used with a factor of safety of 10. Although the outlet side of the valve and the nozzle are only exposed to pressure for short periods, both are also designed with minimum factors of safety of 5. As such, the CGT prototype is well-protected against a pressure-vessel-type failure.

In addition to an appropriate factor of safety against the pressurized gas, the system should also be protected against impact in the case of a fall (i.e., in the case the CGT is unable to prevent a fall). Although design of a structure to protect and encase the CGT is beyond the scope of this feasibility assessment, the CGT as shown in Fig. 3-1 will require shrouding in a protective and presumably padded structure. The protective structure should both protect the user in the event of a fall, and also protect the CGT

components. It should be noted, that in the event of impact with ground, the pressurized gas in the CGT should be fully expended prior to the impact event.

4.5. CGT Embedded System and Control Hardware

An embedded system was designed and constructed to provide sensing and control of the CGT prototype. The embedded system includes a microcontroller (Microchip DSPIC33FJ64GS608-50I/P) for control and communication; a six-axis IMU (TDK InvenSense MPU-6050) and magnetic encoder for feedback control; a brushless motor driver (i.e., MOSFET-based three-phase bridge) and single-quadrant MOSFET amp to drive the brushless motor and solenoid, respectively. The board also provides a CAN interface for real-time communication with a MATLAB Simulink real-time environment at 1 kHz, which was used to implement high-level control of the CGT prototype (subsequently described). The board and the solenoid are powered by 12 v and 26 v benchtop DC power supplies, respectively, for the experimental prototype.

5. CGT Control

5.1. Control Approach for the Feasibility Experiments

In order to evaluate the CGT prototype for control authority, a controller is required to adjust the magnitude of the thrust impulse. Note that the objective of the controller (and the CGT prototype) is not to regulate posture about an equilibrium point. Rather, in the event of an impending fall, the intent is to provide a corrective force impulse that assists the user in returning to their LOS. In the scenario of the backward fall experiments, for example, each of the falling subjects would not have been able to recover from the fall, had corrective assistance not been provided. It is unlikely, however, that the person providing assistance was doing so according to a position control or balance regulation rubric; rather, they provided a corrective force pulse sufficient to arrest the fall and help the (imbalanced) user return to their LOS.

In order to conduct experiments assessing the prospective value of the CGT prototype in helping to arrest a fall, a preliminary control system was developed to

adjust the amount of corrective impulse provided by the CGT. The control system uses an approximate model of a backward falling user in order to apply a force of an appropriate magnitude, rather than attempt to regulate the user to an upright posture. Instead of modulating the thrust magnitude during the relatively short thrust event (which would require an extremely fast servo system), the controller uses a nominal model of the falling human to estimate an appropriate amount of thrust magnitude to provide as a function of the measured tilt angle (i.e., body angle in the sagittal plane). Based on the known properties of the thruster, the controller maintains the nozzle angle that will provide the desired orthogonal thrust that will return the user to their BOS, without overcorrecting and pushing them beyond it. As such, the control philosophy is to always "pre-configure" the nozzle angle to arrest a fall; once a fall condition is detected, as determined by a supervisory controller, the nozzle angle remains at the current setting, and the thrust is triggered by energizing the solenoid. This control approach lessens considerably the bandwidth and torque requirements associated with nozzle servo control, since the nozzle angle is positioned prior to the thrust event (i.e., prior to opening the valve), which enables a relatively small and lightweight servo motor, given the substantial corrective forces required for this application. The following subsections describe the nominal model employed in the experimental controller, and the manner in which it is used for control of the CGT.

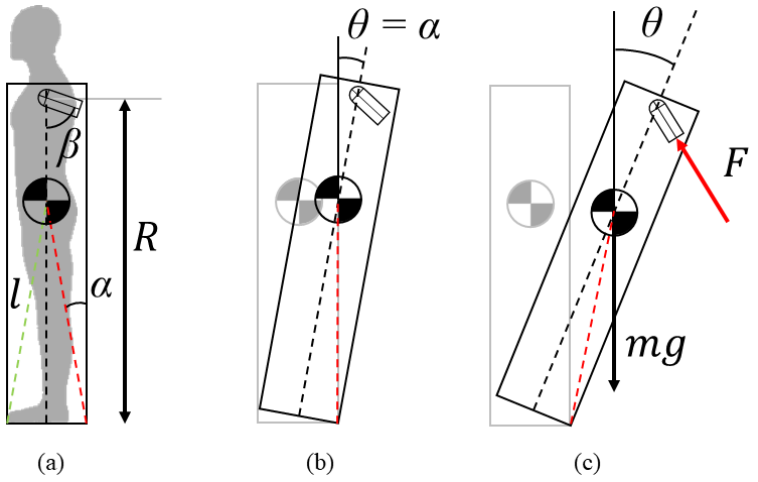

Figure 3-9. Rocking block when (a) stationary, (b) at fall angle, (c) falling.

5.2. Model of a Standing Human

An inverted pendulum model has shown its utility in analyzing human balance [30-31] and balance control [12, 14]. For purposes of assessing the control authority of the CGT prototype, the authors employed instead a "rocking block" model as a simple approximation of a standing human. Unlike an inverted pendulum, a rocking block has a region of stability in which the block remains upright, similar to the LOS of a standing human (see Fig. 3-9). That is, like a standing human, a rocking block inherently has a base of support, and therefore a basin of stability (BOS, equivalent to LOS of a standing human). If the center of mass (COM) of the block is displaced within the BOS, the block will return to stable standing; if the COM is displaced outside the BOS, the block will fall. The angle α that divides these two regions is referred to as the "fall angle" throughout this paper.

A free body diagram of a rocking block is shown in Fig. 3-9. The lines in the diagram are two imaginary pendulums of length l, with negative θ in green, and positive θ in red. The CGT is attached to the rocking block at height R with the nozzle oriented at an angle β with respect to the block vertical axis in the sagittal plane. The motion of the block can be described by

$$\ddot{\theta}(t) = \frac{mgl}{I}\sin(\theta(t) - sign(\theta(t))\alpha) - \frac{R}{I}F(t)\sin(\beta), \qquad (2)$$

where the moment of inertia and mass of the block are denoted by I and m, g is the gravity constant, and F is the magnitude of the CGT-generated thrust given by Eq. (1). Note that Eq. (2) does not account for energy losses from impact as the block hits the ground while rocking, although these losses are not relevant for purposes of estimating the desired assistive force.

5.3. Nozzle Controller

When an impending fall is detected (i.e., for purposes of this feasibility study, when the rocking block is in a configuration outside of its basin of stability), the objective

of the CGT system is to exert a force that will return the block to within the basin of stability. Assuming thrust along the major axis of the rocking block is a non-working force, the component of corrective thrust applied by the CGT can be controlled by rotating the nozzle angle relative to the vertical. As dictated by the control approach described earlier, the nozzle does not change orientation during the thrust event (i.e., the nozzle angle is configured prior to the fall event and kept constant during the thrust event). Thus, the control problem becomes estimating the appropriate magnitude of the provided thrust to restore the system to stability; namely, to propel the block from some initial angle ($\theta = \theta_0 > \alpha$) to the edge of its basin of stability ($\theta = \alpha$), after which it is assumed to "recover" naturally. A closed form solution for the nozzle angle can be obtained by first linearizing Eq. (2). The equation of motion has two nonlinearities: the discontinuity at θ zero crossing, described by the signum function, and the sine function. The motion from θ_0 to α does not involve zero crossings, so the model can be treated as an inverted pendulum by substituting the quantity $\theta - \alpha$ with the pendulum angle q and $\dot{\theta}$ with $\dot{q}$. The objective then becomes bringing the block from $q_0 = \theta_0 - \alpha$ to zero. The sine function can be linearized around the operating point q_L such that:

$$\tilde{\ddot{q}}(t) = A_1 q(t) + A_2 + A_3 F_{max} e^{-t/\tau} \sin(\beta), \tag{3}$$

where $A_1 = mgl \cos q_L / I$, $A_2 = mgl(\sin q_L - q_L \cos q_L)/I$, $A_3 = -R/I$, and $\tilde{\ddot{q}}$ is the linearized approximation of Eq. (2). This expression was linearized about a pendulum angle q_L=13 deg, which is approximately the mid-point of the CGT control authority, as presented later in this paper. Given the initial conditions q_0, $\dot{q}_0$, the closed form solution of the linearized model can be expressed as:

$$\tilde{q}(t) = B_1 + B_2 e^{-t/\tau} + B_3 \cosh(Mt) + B_4 \sinh(Mt), \tag{4}$$

where $M = \sqrt{mgl \cos q_L / I}$, $B_1 = q_L - \tan q_L$, $B_2 = -RF_{max} \sin(\beta) / (I\tau^{-2} - IM^2)$, $B_3 = q_0 - B_1 - B_2$, and $B_4 = \left(\dot{q}_0 + {}^{B_2}/_{\tau}\right)/M$. Knowing the time length of the force pulse t_f, the desired final condition $q(t_f) = \dot{q}(t_f) = 0$, the nozzle angle β can be calculated as:

$$\beta = \sin^{-1}\frac{C_1 I\left(\tau^{-2}-M^2\right)}{C_2 R F_{max}}, \tag{5}$$

where $C_1 = B_1 + (q_0 - B_1)\cosh(Mt_f) + {\dot{q}_0}/{M}\sinh(Mt_f)$ and $C_2 = e^{-t_f/\tau} - \cosh(Mt_f) + {1}/{(\tau M)}\sinh(Mt_f)$. Therefore, for the purposes of assessing the control authority of the CGT prototype to correct an impending fall as proposed here, the control law expressed by Eq. (5) was employed to compute the nozzle angle of the CGT as a function of tilt angle. The extent to which this controller might be effective in a modified form to use with a falling human user is a topic of future work. Similarly, a corresponding supervisory controller, which will be required to detect an impending fall and subsequently energize the solenoid, is also a topic of future work.

6. Experimental Assessments

6.1. Thrust Validation

In order to confirm that the CGT prototype provides the nominal thrust characteristics for which it was designed, the assembled prototype was mounted on a force plate (AMTI Optima, Watertown, MA), with the nozzle pointing vertically upward, such that the resultant thrust force was directed vertically downward into the floor. The thrust magnitude was recorded during five trial "firings" and compared to the expected thrust predicted by Eq. (1). Figure 3-10 shows measured force corresponding to each of the five individual thrust trials (light blue) and the corresponding average (black). The solid red line is the analytically predicted thrust, which matches well with the average measured thrust curve temporally. As can be observed in the figure, however, the average measured thrust is somewhat lower than the predicted thrust, due to simplifying assumptions in the flow model (e.g., assumption of constant temperature of the gas during the thrust event) and unmodelled flow losses, such as the loss due to the pressure drop across the tank exit and valve throat. As such, an empirically-determined loss coefficient of 0.9 was included in the control law, which resulted in a close match between the adjusted theoretical and measured thrust curves, as shown by the red

dashed line in Fig. 3-10. Based on this validation of the CGT output, the authors constructed a subsequent experiment to assess the extent to which the controlled CGT could provide forces sufficient to arrest and counteract an impending fall.

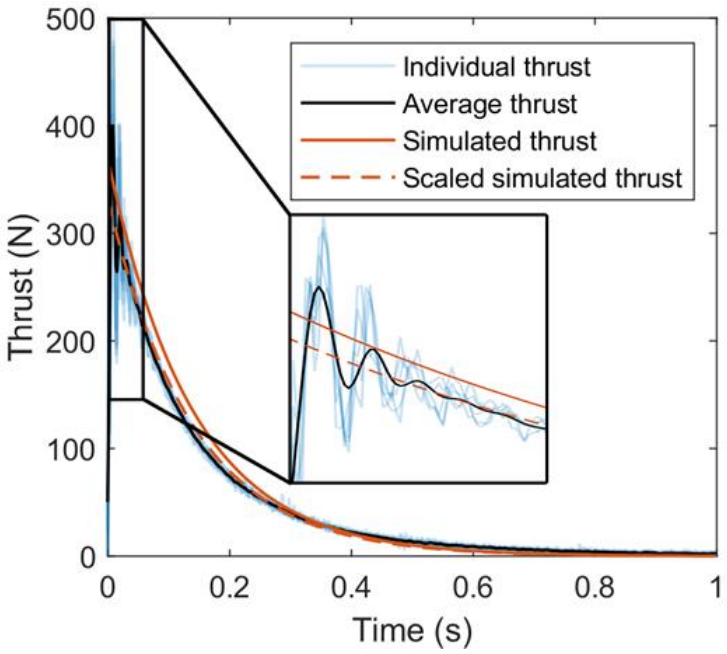

Figure 3-10. Analytically predicted and experimentally measured CGT thrust curves.

6.2. Rocking Block Experiment

The authors assessed the preliminary functionality of the CGT and control approach on a rocking block experimental apparatus, in order to isolate the corrective effects of the CGT relative to a human user, and to avoid risks associated with testing the early-stage prototype on human participants. The experimental rocking block apparatus, with the CGT mounted, is shown in Fig. 3-11. The rocking block is comprised of a vertical steel shaft welded to a steel baseplate, upon which fitness weights are mounted. The shaft is 1.37 m long and 5 cm in diameter, and the baseplate is 20 cm x 38 cm x 0.64 cm (8 in x 15 in x 0.25 in). The width of the baseplate, along with the height of the COM, determines the fall angle in the sagittal plane. The baseplate was constructed as rectangle to reduce rocking in the frontal plane. The total mass of the unweighted structure is approximately 8.5 kg (19 lb); for the experiments described here, a total

mass of 45.5 kg (100 lb) of fitness weights was placed on the shaft and clamped at a height of 0.82 m above the floor, while the CGT prototype was clamped to the shaft at a height of 1.24 m above the floor. With the combined mass and mass distributions of the structure and fitness weights, the complete apparatus had a mass of approximately 54 kg (119 lb); COM located approximately 0.75 m above the floor; and a resultant fall angle (i.e., LOS) of 7.6 deg.

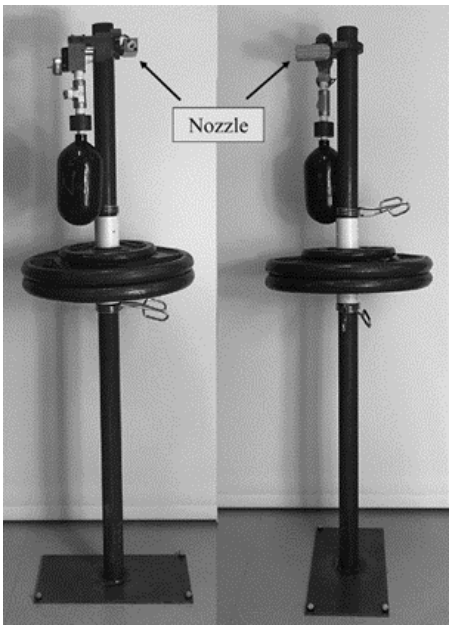

Figure 3-11. CGT on the rocking block (front and side views), with the nozzle shown at a nozzle angle of 90 deg.

For the experimental setup shown in Fig. 3-11, the response of the rocking block was measured when released from a series of initial angles, with and without CGT assistance. For the case without assistance, the rocking block was held at an initial angle and released from rest, while the angle of the base plate relative to the horizontal was measured using a motion capture system (Vicon, Oxford GBR). The angle of the base plate was used rather than the shaft to mitigate the potential for structural vibration in the measurement. The block was released from 7 different angles, approximately evenly spaced between 5 and 25 deg. An overhead harness was attached to the top of the shaft of the rocking block, which was slack until the block reached an angle of approximately

35 deg, at which point the harness caught the apparatus to prevent it from hitting the floor.

Following the assessment of the baseline (i.e., unassisted) dynamics, the CGT was mounted to the experimental apparatus, and the same essential protocol was followed, but with two primary differences. First, rather than release the apparatus by hand, the apparatus was suspended at an initial angle by the overhead harness, while the CGT was activated remotely, which was implemented to reduce the potential for interference with the initial condition. Second, seven initial angles were selected approximately evenly spaced between approximately 13 and 26 deg (i.e., the region in which the unassisted block would fall). This range of angles was selected primarily based on simulations, which predicted the CGT would provide recovery through this range.

Recall that the intent of the CGT is to provide a corrective force to prevent a fall in a manner that will return the user's COM into the LOS; the device, however, is not intended to explicitly regulate balance once the COM is within the LOS. Experiments were conducted on a steel floor in a motion capture lab, and in preliminary experiments, the apparatus rocked for approximately 7 s before settling. In order to better represent the time scale of a self-stabilizing human response, the authors inserted a 12-mm-thick sheet of viscoelastic material (Sorbothane) between the plate and floor, reducing the coefficient of restitution to approximately 0.7 (originally 0.9 without the Sorbothane), which resulted in a more representative settling time of 2.5 s [32]. An anti-slip pad was also used between the Sorbothane and floor to mitigate sliding.

For the cases with CGT assistance, the 1 L CGT tank was charged with 10 MPa (1500 psi) of nitrogen gas from a standard nitrogen tank through a flexible hose which included a manual shut-off valve. Prior to each experiment, the one-liter CGT tank was charged with gas and the shut-off valve turned off, disconnecting the CGT tank from the larger nitrogen tank. However, the flexible hose connecting the nitrogen and CGT tanks was left connected to prevent the need to disconnect and reconnect high-pressure fittings between each trial. Based on measured responses, the flexible hose did not noticeably affect the response of the block.

Although the response of the block was measured using the Vicon camera-based system, the CGT used only on-board sensing for control (i.e., the on-board IMU). In order to streamline controller implementation for these experiments, the embedded system was connected via a CAN bus to a host computer running the real-time MATLAB/Simulink environment. A control loop was run at 1 kHz, where tilt angle was computed on the embedded system and sent via CAN to the host computer; the nozzle angle was computed on the host computer and returned to the embedded system; and the embedded system implemented the nozzle command via the servomotor. For each experimental case, the control law was computed, and the corrective thrust was triggered by energizing the valve solenoid.

It should be noted that, for the case without assistance, the CGT prototype was not mounted to the block, which changed slightly the dynamic characteristics of the block. Without the CGT, the mass of the rocking block was 54 kg and COM located 0.75 m above the floor. With the CGT, the mass was 56 kg and COM 0.76 m above the floor which reduced the fall angle to 7.5 deg.

A video demonstrating the experiments for both cases (with and without assistance) is available at https://youtu.be/NCM43QYHNA0. A sequence of frames from the experimental video is shown in Fig. 3-12, which shows the block: 1) at initial conditions; 2) approximately 400 ms after energizing the CGT; 3) the block rocking within its region of stability; and 4) the block settled to its equilibrium position.

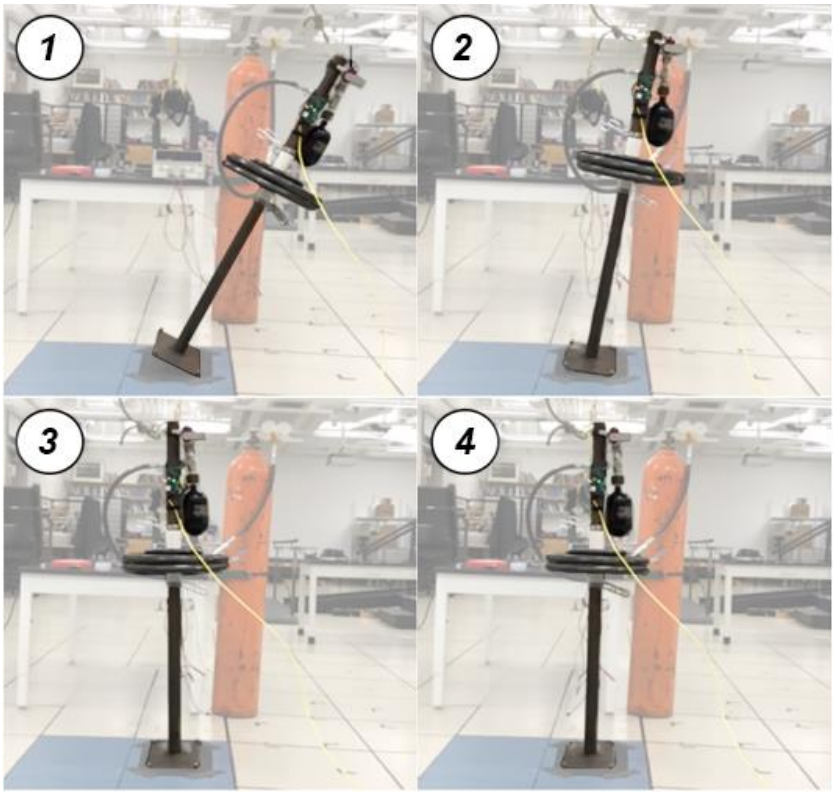

Figure 3-12. Frames from a video (available at https://youtu.be/NCM43QYHNA0) of an experimental trial with CGT assistance, showing the apparatus: (1) at the initial state, in this case at a 25.5 deg tilt angle; (2) shortly after energizing the solenoid; (3) returned to the basin of stability; and (4) settled in an upright position. Note that the nozzle angle is 90 deg in this case, since this is the maximum tilt angle from which the system can recover. The images were mirrored from the original video to align with the directional conventions of the paper.

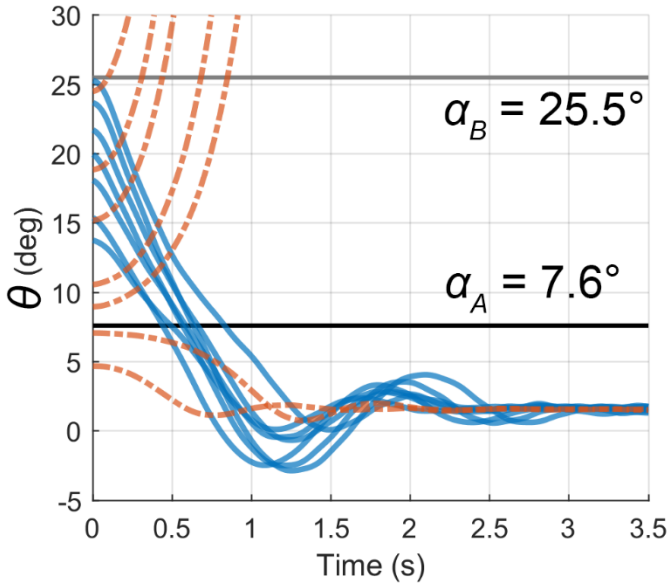

Figure 3-13. Measured rocking block tilt angle shown without (dashed red) CGT assistance, and when using the CGT to restore the block to its basin of stability (solid blue line).

7. Results and Discussion

7.1. Control Authority

The results of the control authority feasibility experiments are shown in Fig. 3-13, with corresponding control (i.e., nozzle angle) commands shown in Fig. 3-14. In Fig. 3-13, the red dashed lines show the response of the block without assistance, and blue solid lines show the block response with CGT assistance. As shown in Fig. 3-13, for the experiments without assistance, the block fell at any initial tilt angle greater than its fall angle (7.6 deg). For the experiments with CGT assistance, the CGT was able to restore the rocking block to its region of stability when released from all initial angles up to 25.5 deg. The 2 kg CGT prototype was therefore able to effectively expand the region of stability substantially, indicating promise as a wearable device for preventing or mitigating falls for people at fall risk.

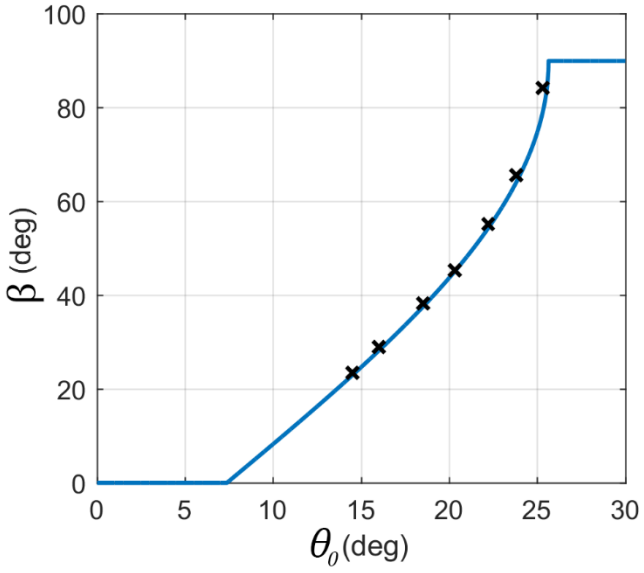

Figure 3-14. Nozzle control angle β as a function of the initial block angle θ_0. Black marks indicate the experiment conditions.

7.2. Limitations of the Feasibility Study

The experiments presented here were intended to assess the extent to which a CGT has the control authority to correct an impending fall. Although the experiments conducted demonstrate real promise in that regard, there is a number of limitations to the work with respect to the intended application. Among these, the experiments described here all started at rest. For any realistic fall, the CGT will likely be employed as the user is falling (i.e., the CGT will be triggered when the user has a non-zero initial velocity). Second, the rocking block model used here is a single-segment body, while a human user is a multi-segment body that will change configuration as a compensatory action well before a tilt angle of 25 deg (i.e., well before the limit tested here). Although both limitations are important, the first limitation actually mitigates the effect of the second. Namely, since much of the CGT thrust is expected to reduce and reverse the initial velocity, the tilt angles at which the CGT would trigger in a "dynamic" fall scenario would be much smaller than the tilt angles examined here. As such, compensatory changes in segment angles would be expected to be small by the time the CGT becomes active in a dynamic, multi-segment fall. Given the control authority of the CGT as

characterized here, along with the narrower range of tilt angles expected with dynamic falls (i.e., falls with an initial velocity), the authors plan in future work to examine the extent to which the CGT will be effective in a modified form to use for dynamic falls, and for dynamic falls with human users. This future work will specifically include development of a supervisory fall-detecting controller, in addition to supporting experiments that address dynamic fall scenarios, along with an exploration of the effect of multi-segment fall modes.

It is worth noting that the intent of the CGT system is to provide a nominally appropriate corrective force that will aid the user in returning to their LOS, in a manner similar to a human assistant. Such a human assistant would presumably be instrumental in arresting a fall, without necessarily employing an exact estimate of corrective force. A falling person will also contribute an effort to restoring their balance, which might reduce both the level of required assistance, and the necessity for precision control. In other words, the CGT is intended to provide assistance to restore balance, rather than balance control, which likely reduces the need for control precision. An examination of the level of precision required of a CGT controller will require human subject experiments, which is a topic of future work.

Finally, an inherent limitation of the design, the CGT as configured here would only have sufficient stored energy to provide for a single major correction per charge of gas. As such, once used to arrest an impending fall, the CGT tank would require recharging prior to subsequent use. Therefore, the device is intended to be utilized as a safety measure, to mitigate or prevent falls that occur infrequently. Such relatively low-frequency use is consistent with the expected frequency of falling in elderly individuals. Specifically, approximately 25% of adults over 65 years of age reported falling in the past year [33]. Of those, approximately half fell once; one quarter fell twice; and one quarter fell three or more times. Although such falls are relatively infrequent, according to [33], “a substantial share of healthcare expenditures for adults aged 65 and older was attributable to [these] falls.”

8. Conclusion

This paper describes the design of a first-of-its-kind CGT, which is intended as a backpack-worn device to arrest or correct falls for individuals at fall risk. The primary purpose of the paper was to present the design of the prototype device, and to assess the feasibility that a device, of appropriate size and weight for a backpack-worn form, could generate sufficient force impulse to arrest an impending fall. Experiments on a rocking block constructed to emulate the falling characteristics of a human indicated that, for a rocking block with a nominal fall angle of 7 deg, use of the CGT was able to restore the block to upright stability for angles up to 26 deg. Such an angle is unrealistic given that the block started at rest; nonetheless, the experiments demonstrate considerable control authority to potentially correct an impending fall. Future work will focus on modifying the controller to accommodate falls with initial velocity; incorporating a supervisory controller to trigger correction when appropriate; assessing the extent to which the controller should be adapted for human use; and subsequently testing on human subjects.

9. Addendum

9.1. Modeling of the CGT Thrust

The CGT-based device considered here generates thrust by releasing the gas stored in the tank through a converging-diverging nozzle. If the flow path of the gas is sufficiently smooth, such that no shock waves and sharp changes in the flow variables occur, the flow can be considered isentropic. It is also supersonic if the tank pressure is above the critical pressure of $1.893*P_{atm}$ (for air or nitrogen) [25]. If both conditions are satisfied, the gas moves at different speeds throughout the path due to compressibility effects. At the narrowest point of the path, commonly referred to as the nozzle *throat*, a phenomenon called *choked flow* takes place, limiting the flow velocity to the speed of sound in the given gas. After passing the throat the gas expands with the nozzle area, accelerating the flow to the maximum speed at the nozzle exit.

Based on these assumptions, equations (6-19) are employed to model the thrust created by a CGT (as described in [25-26]). First, the throat pressure P_t and temperature T_t can be calculated from the tank pressure P_0 and temperature T_0 using (6-7), where γ is the specific heat ratio of the gas. The gas density at the throat ρ_t is found in (8), where R is the specific gas constant.

$$P_t(t) = \frac{P_0(t)}{\left(1+\frac{\gamma-1}{2}\right)^{\frac{\gamma}{\gamma-1}}} \tag{6}$$

$$T_t = \frac{T_0}{1+\frac{\gamma-1}{2}} \tag{7}$$

$$\rho_t(t) = \frac{P_t(t)}{T_t R} \tag{8}$$

The flow velocity v_t at the throat, which due to choked flow is equal to the speed of sound in a given gas, can be computed using (9). The throat area A_t and the flow velocity can be used to compute the mass flow rate $\dot{m}$, which is constant throughout the system (10).

$$v_t = v_{sound} = \sqrt{\gamma T_t R} \tag{9}$$

$$\dot{m}(t) = \rho_t(t) v_t A_t \tag{10}$$

Equation (11) is used to find the flow velocity at the nozzle exit in Mach units M_e that corresponds to the maximum obtainable thrust, assuming ideal nozzle design and constant tank pressure. However, since the tank pressure diminishes with time, the nozzle design is not ideal for t > 0, which is explained in more detail in the next section.

$$M_e(t) = \left(\frac{2}{\gamma-1}\right)^{1/2}\left(\left(\frac{P_0(t)}{P_{atm}}\right)^{\frac{\gamma-1}{\gamma}} - 1\right)^{1/2} \quad (11)$$

The pressure P_e, temperature T_e, and gas density ρ_e at the nozzle exit are computed in (12-14) and are used to calculate the exit flow velocity v_e (15), based on the given exit area and the fact that the mass flow rate is the same at all points in the flow path.

$$P_e(t) = \frac{P_0(t)}{\left(1+M_e(t)^2\frac{\gamma-1}{2}\right)^{\frac{\gamma}{\gamma-1}}} \quad (12)$$

$$T_e(t) = \frac{T_0}{1+M_e(t)^2\frac{\gamma-1}{2}} \quad (13)$$

$$\rho_e(t) = \frac{P_e(t)}{T_e(t)R} \quad (14)$$

$$v_e(t) = \frac{\dot{m}(t)}{\rho_e(t)A_e} \quad (15)$$

Finally, for flow conditions at the exit, the thrust F can be found as:

$$F(t) = \dot{m}(t)v_e(t) + A_e(P_e(t) - P_{atm}) \quad (16)$$

Since the CGT-based device considered here will employ a blow-down tank of cold gas, the tank pressure and subsequently the thrust will drop to zero exponentially. This decay can be modeled as follows. The initial mass of the gas m(t=0) can be calculated as:

$$m(0) = \frac{P_0(0)V_0}{RT_0} \quad (17)$$

Once the flow path is opened, the mass left in the tank over time can be described by (18), where $\dot{m}(t)$ is the mass flow rate computed in (10).

$$m(t) = m(0) - \dot{m}(t)t \tag{18}$$

As gas leaves the tank, the tank pressure continually drops according to (19) until P_0 drops below the critical pressure, turning the flow to subsonic, and eventually equalizes with the atmospheric pressure, bringing the thrust down to zero. The variables in (6-16) are continually updated with the changing tank pressure.

$$P_0(t) = \frac{m(t)RT_0}{V_0} \tag{19}$$

9.2. Selecting the nozzle geometric parameters

While we are relatively free in selecting the tank pressure and the nozzle throat radius, the nozzle exit radius can be optimized to produce maximum obtainable thrust. Assuming isentropic and supersonic flow, the speed of flow in Mach units M at any point inside the nozzle can be related to the cross-sectional area of the nozzle at that point A_e with

$$\frac{A_e}{A_t} = \frac{1}{M}\left(\frac{\gamma+1}{2}\right)^{-\frac{\gamma+1}{2(\gamma-1)}}\left(1 + M^2\frac{\gamma-1}{2}\right)^{\frac{\gamma+1}{2(\gamma-1)}}. \tag{20}$$

This relationship is graphed in Fig. 3-15 on the left axis as a blue dotted line for a nozzle with a throat diameter from Table 3-1. For constant pressure (or pressure at a moment in time), thrust was calculated for each point on the x-axis, plugging M into (12-16) instead of M_e. Each red solid line is the thrust-Mach curve for different pressure conditions decreasing with the line opacity. For each pressure, the flow velocity resulting in the maximum thrust, denoted by a point on the red curve, is M_e from (11). Knowing the optimal area ratio causing this velocity and the nozzle throat area, the optimal exit area can be calculated from (20). As gas leaves the tank, the tank pressure

goes through all pressures below it, and as Fig. 3-15 demonstrates, the optimal area ratio shifts left on the plot. Since maximum thrust occurs at maximum pressure, the corresponding nozzle exit area was used.

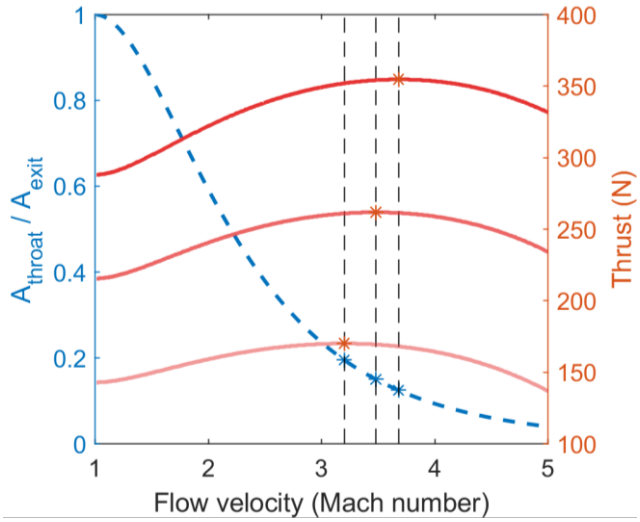

Figure 3-15. Area ratio (blue dotted) and thrust (red solid) for pressure from 10 MPa (darkest) to 5 MPa (lightest).

This model was simulated in MATLAB Simulink (MathWorks, Natick, MA) to study the thrust as a function of the design variables. For the selected nozzle throat radius and varying initial pressure, the thrust curves over time are shown in Fig. 3-16(a). The time constant of the thrust decay remains the same, while the amplitude is directly proportional to the initial pressure.

On the other hand, larger nozzle throat area results in a higher thrust that diminishes quickly, whereas a smaller area produces a smaller thrust over longer period of time, as depicted in Fig. 3-16(b). Additional constraint on the nozzle throat radius is that the flow path cross-sectional area needs to be significantly larger than the throat area for choking to occur. Based on the flow path area, limited by the fittings and tubes available, the response speed of the valve constructed for this study, and general consideration of keeping the loads in the system safe and manageable, the nozzle throat radius r_t was chosen to be 2.7 mm (red thrust curve in Fig.3-16(b)). This nozzle throat radius results in a thrust profile closely matching the force profile from Fig. 3-3. The

nozzle exit radius r_e was calculated using the optimal area ratio from (20) and is equal to 7.7 mm. Knowing these parameters and the parameters in Table 3-1, the peak thrust $F(t=0)$ was anticipated to be approximately 370 N with the total thrust duration of around 0.7 s.

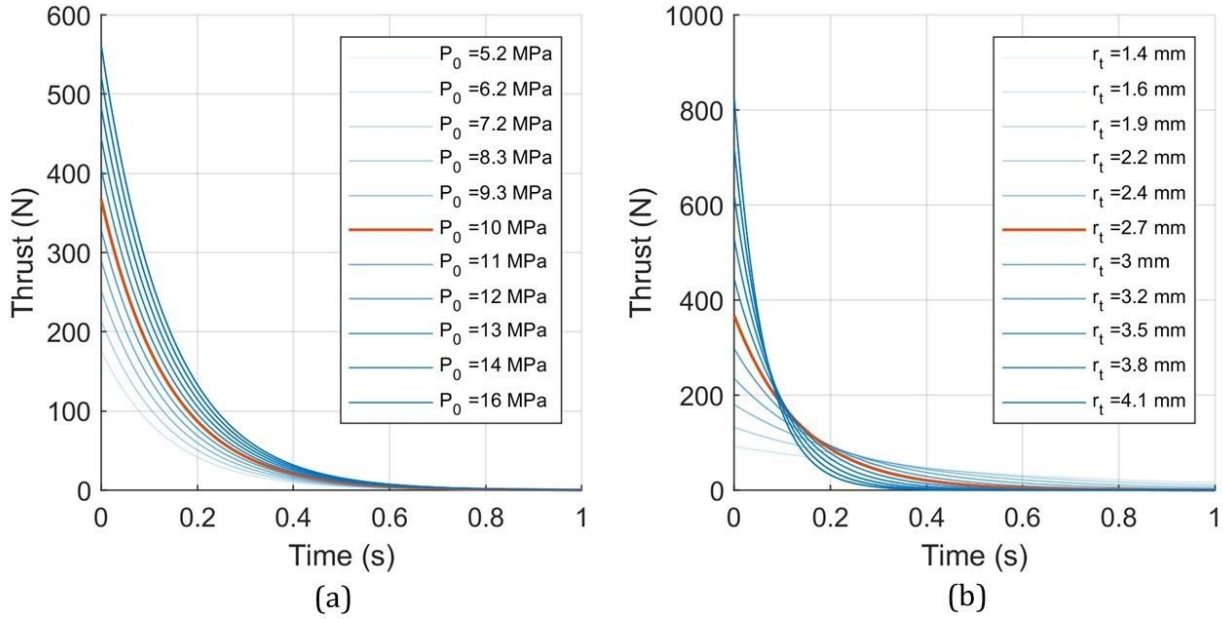

Figure 3-16. Thrust generated by (a) various pressures with nozzle throat radius 2.7 mm (area ratio = 8.13, Mach number = 3.7), (b) various nozzle throat radii at 10 MPa.

10. References

[1] Ambrose, A. F., Paul, G., and Hausdorff, J. M., 2013, "Risk factors for falls among older adults: a review of the literature," *Maturitas*, 75(1), pp. 51–61, doi: 10.1016/j.maturitas.2013.02.009.

[2] Bergen, G., Stevens, M. R., and Burns, E. R., 2016, "Falls and Fall Injuries Among Adults Aged ≥65 Years — United States, 2014," *MMWR Morb. Mortal. Wkly. Rep*., 65(37), pp. 993–998, doi: 10.15585/mmwr.mm6537a2.

[3] Lockhart, T. E., Smith, J. L., and Woldstad, J. C., 2005, "Effects of Aging on the Biomechanics of Slips and Falls," *Hum. Factors J. Hum. Factors Ergon. Soc*., 47(4), pp. 708–729, doi: 10.1518/001872005775571014.

[4] Lord, S. R., Ward, J. A., Williams, P., and Anstey, K. J., 1993, "An epidemiological study of falls in older community-dwelling women: the Randwick falls and fractures study," *Aust. J. Public Health*, 17(3), pp. 240–245, doi: 10.1111/j.1753-6405.1993.tb00143.x.

[5] Hamza, M. F., Ghazilla, R. A. R., Muhammad, B. B., and Yap, H. J., 2020, "Balance and stability issues in lower extremity exoskeletons: A systematic review," *Biocybernetics and Biomedical Engineering*, 40 (4), pp. 1666–1679, doi: 10.1016/J.BBE.2020.09.004.

[6] Tucker, M.R., Olivier, J., Pagel, A., et al., 2015, "Control strategies for active lower extremity prosthetics and orthotics: a review," *J Neuroeng. Rehabil*, 12(1), https://doi.org/10.1186/1743-0003-12-1

[7] T. Yan, M. Cempini, C. M. Oddo, and N. Vitiello, 2015, "Review of assistive strategies in powered lower-limb orthoses and exoskeletons," *Rob. Auton. Syst.*, vol. 64, pp. 120–136, doi: 10.1016/j.robot.2014.09.032.

[8] Wang, S., et al., 2015, "Design and Control of the MINDWALKER Exoskeleton," *IEEE Trans. Neural Syst. Rehabil. Eng.*, 23(2), pp. 277–286, doi: 10.1109/TNSRE.2014.2365697.

[9] Zhang, T., Tran, M., and Huang, H., 2018, "Design and experimental verification of hip exoskeleton with balance capacities for walking assistance," *IEEE/ASME Trans. Mechatronics*, 23(1), pp. 274–285, doi: 10.1109/TMECH.2018.2790358.

[10] Ugurlu, B., et al., 2016, "Variable Ankle Stiffness Improves Balance Control: Experiments on a Bipedal Exoskeleton," *IEEE/ASME Trans. Mechatronics*, 21(1), pp. 79–87, doi: 10.1109/TMECH.2015.2448932.

[11] Fasola, J., Vouga, T., Baud, R., Bleuler, H., and Bouri, M., 2019, "Balance control strategies during standing in a locked-ankle passive exoskeleton," *IEEE Int. Conf. Rehabil. Robot.*, pp. 593–598, doi: 10.1109/ICORR.2019.8779500.

[12] Huynh, V., Bidard, C., and Chevallereau, C., 2018, "Balance control for an active leg exoskeleton based on human balance strategies," *Mech. Mach. Sci.*, 48, pp. 197–211, doi: 10.1007/978-3-319-59972-4_15.

[13] Di, P., et al., 2016, "Fall detection and prevention control using walking-aid cane robot," *IEEE/ASME Trans. Mechatronics*, 21(2), pp. 625–637, doi: 10.1109/TMECH.2015.2477996.

[14] Vallery, H., Bögel, A., O´Brien, C. and Riener, R., 2012, "Cooperative Control Design for Robot-Assisted Balance During Gait," *Auto*., 60 (11), pp. 715-720, doi: 10.1524/auto.2012.1041.

[15] Chiu, J., and Goswami, A., 2014, "Design of a Wearable Scissored-Pair Control Moment Gyroscope (SP-CMG) for Human Balance Assist," *Volume 5A: 38th Mechanisms and Robotics Conference*, Buffalo, NY, USA, p. V05AT08A023, doi: 10.1115/DETC2014-35539.

[16] Lemus, D., van Frankenhuyzen, J., and Vallery, H., 2017, "Design and Evaluation of a Balance Assistance Control Moment Gyroscope," *J. Mech. Robot*., 9(5), p. 051007, doi: 10.1115/1.4037255.

[17] Li, D., and Vallery, H., 2012, "Gyroscopic assistance for human balance," *12th IEEE International Workshop on Advanced Motion Control (AMC)*, Sarajevo, Bosnia and Herzegovina, pp. 1–6, doi: 10.1109/AMC.2012.6197144.

[18] Matsuzaki, R., and Fujimoto, Y., 2013, "Walking assist device using Control Moment Gyroscopes," *IECON 2013 – 39th Annual Conference of the IEEE Industrial Electronics Society*, Vienna, Austria, pp. 6581–6586, doi: 10.1109/IECON.2013.6700220.

[19] Oya, H., and Fujimoto, Y., 2017, "Preliminary experiments for postural control using wearable-CMG," *Proceedings IECON 2017 – 43rd Annual Conference of the IEEE Industrial Electronics Society*, pp. 7602–7607, doi: 10.1109/IECON.2017.8217332.

[20] Lemus, D., et al., 2020, "Controller synthesis and clinical exploration of wearable gyroscopic actuators to support human balance," *Sci. Rep*., 10(1), pp. 1–15, doi: 10.1038/s41598-020-66760-w.

[21] Alexander, N. B., 1994, "Postural Control in Older Adults," *J. Am. Geriatr. Soc*., 42(1), pp. 93–108, https://doi.org/10.1111/j.1532-5415.1994.tb06081.x.

[22] Maki, B. E., McIlroy, W. E., and Fernie, G. R., 2003, "Change-in-support reactions for balance recovery," *IEEE Engineering in Medicine and Biology Magazine*, 22(2), pp. 20-26, doi: 10.1109/MEMB.2003.1195691.

[23] Tan, J. S., Eng, J. J., Robinovitch, S. N., and Warnick, B., 2006, "Wrist impact velocities are smaller in forward falls than backward falls from standing," *Journal of Biomechanics*, 39(10), pp. 1804–1811, doi: 10.1016/j.jbiomech.2005.05.016.

[24] King, M. B., Judge, J. O., Wolfson, L., 1994, "Functional base of support decreases with age," *Journal of Gerontology*, 49(6), pp. M258-63. DOI: 10.1093/geronj/49.6.m258.

[25] Cantwell, B. J., 2018, *AA210A Fundamentals of Compressible Flow*, Stanford University, Stanford, CA.

[26] Potter, M. C., and Foss, J. F., 1982, *Fluid mechanics*, Ronald Press Co., New York, NY.

[27] Finn-Henry, M., Baimyshev, A., and Goldfarb, M., 2020, "Feasibility Study of a Fall Prevention Cold Gas Thruster," *8th IEEE RAS/EMBS International Conference for Biomedical Robotics and Biomechatronics (BioRob)*, pp. 611-616, doi: 10.1109/BioRob49111.2020.9224425.

[28] Anis, A., 2012, "Cold Gas Propulsion System - An Ideal Choice for Remote Sensing Small Satellites," *Remote Sens. - Adv. Tech. Platforms*, doi: 10.5772/37149.

[29] Singh, J., Zerpa, L. E., Partington, B., and Gamboa, J., 2019, "Effect of nozzle geometry on critical-subcritical flow transitions," *Heliyon*, 5(2), p. e01273, doi: 10.1016/j.heliyon.2019.e01273.

[30] Hof, A. L., 2008, "The 'extrapolated center of mass' concept suggests a simple control of balance in walking," *Human Movement Science*, 27 (1), pp. 112–125, doi: 10.1016/j.humov.2007.08.003.

[31] Pai, Y. C., and Patton, J., 1997, "Center of mass velocity-position predictions for balance control," *Journal of Biomechanics*, 30 (4), pp. 347–354, doi: 10.1016/s0021-9290(96)00165-0.

[32] Piirainen, J. M., Linnamo, V., Cronin, N. J., and Avela, J., 2013, "Age-related neuromuscular function and dynamic balance control during slow and fast balance perturbations," *J. Neurophysiol*., 110(11), pp. 2557–2562, doi: 10.1152/jn.00476.2013.

[33] Florence, C. S., Bergen, G., Atherly, A., Burns, E., Stevens, J., and Drake, C., 2018, "Medical Costs of Fatal and Nonfatal Falls in Older Adults," *J. Am. Geriatr. Soc*., 66(4), pp. 693–698, doi: 10.1111/jgs.15304.

CHAPTER 4

COLD-GAS THRUSTER BASED FALL PREVENTION DEVICE: EXPLORING DYNAMIC FALLS

1. Introduction

The model-based nozzle controller, presented in the Chapter 3, approximates the balance dynamics of the user using a rocking block model with the user's physical parameters (mass, COM position, and moment of inertia) and the tilt angle of the block to calculate the force that is necessary to displace the block from the given tilt angle to an upright equilibrium. Supporting experiments were designed in that chapter to assess only the capabilities and limits of the initial CGT prototype at zero initial velocity. In that chapter, the block was configured outside its limits of stability (LOS) and held stationary prior to triggering the device. In a more realistic scenario, however, a person's body starts accelerating the falling motion immediately after leaving their LOS and will have some velocity at any angle outside the LOS. In order to consider this more realistic case, experiments with non-zero initial velocity were conducted to inform the assessment of the CGT. Additionally, the previous work did not include a controller or algorithm that determines when to initiate firing of the CGT, since the experiments were designed to explore different static snapshots of block states, which did not require real-time decision-making. As such, these dynamic experiments also tested an autonomous supervisory controller, developed in this chapter.

For the purposes of this study, a new prototype of the CGT, shown in Fig. 4-1, was designed and constructed. The valve topology remained the same, although the component designs were improved to increase robustness. The servo system was isolated from the flow path to reduce the leaks when generating thrust, and a tensioned belt transmission was used instead of spur gears to reduce backlash. These changes improved the efficiency and the repeatability of the CGT and increased the peak thrust

output of the system by 16%. This prototype was used in the experiments described in this chapter.

The proposed supervisory controller tracks the states of the user to predict potential falls and trigger the CGT when an onset of a fall is detected. A metric for assessing the balance condition of the user is introduced, which relies on the states of the block, namely the angle from vertical and angular velocity, to predict a fall. If the state configuration remains within some boundary in the phase space, the block recovers upright equilibrium on its own; otherwise, a fall is initiated. The region encompassed by this boundary is referred to as the stability basin (SB) throughout this chapter. The CGT can potentially expand the inherent SB of the block by applying assistive thrust and returning the block to equilibrium from state configurations outside its inherent SB. The boundaries of this CGT-expanded SB are explored through simulation and validated experimentally in this chapter. Furthermore, to address the applicability of the presented CGT supervisory controller to a human user, key differences between the rocking block model and a human body are identified. Simulations are performed on a three-segment model of a human body with ankle and hip joints to gauge the dynamic response of the model to the CGT intervention. Finally, some remarks are provided regarding the potential changes to the CGT instrumentation and the controller necessary for use with human users.

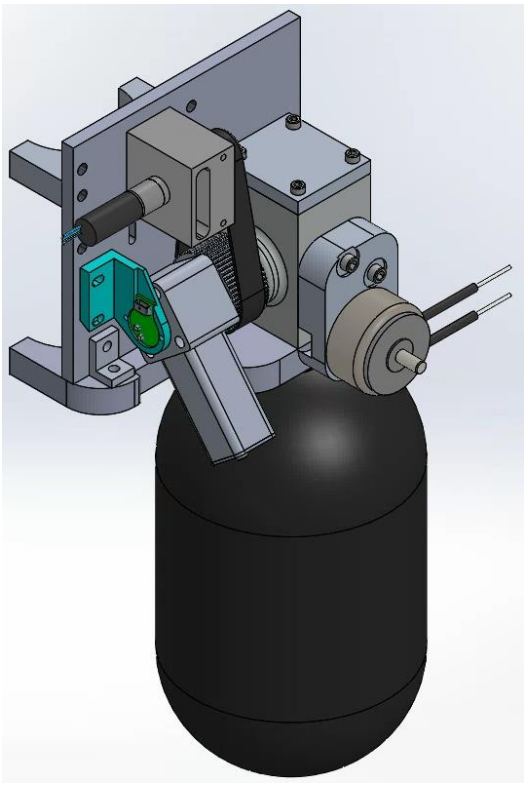

Figure 4-1. CGT prototype v2 in CAD.

2. CGT Supervisory Controller

The responsibilities of the supervisory controller include (a) detecting an onset of a fall and (b) selecting an appropriate time to apply assistance.

2.1. Fall detection

A literature search was performed in the field of human fall detection, mainly focused on the elderly population. The majority of proposed approaches to detect falls are based on wearable sensors, such as accelerometers and gyroscopes, external or ambient visual sensors, such as RGB and/or depth cameras with feature tracking (not feasible for the mobile wearable CGT), or the combination of the two, sometimes augmented with vital signal sensors [1-7]. However, the main objective of fall detection systems in these works is predominantly to inform emergency services if a person falls and loses autonomy. As such, the two main sources of information for wearable sensors

are the fall impact, which produces a distinguishable spike in acceleration signals, and the horizontal position of the body for an extended period after the fall. For the purposes of the CGT, these fall detection systems are not acceptable since the aim of the CGT is to prevent the fall, and therefore the impending fall must be detected well before impact or considerable deviation from the upright posture. Nyan et al. [8] propose a pre-impact fall detection for use with inflatable hip protectors, although the detection occurs past the limits of control authority of the proposed device. Therefore, the CGT supervisory controller requires a method of fall prediction, rather than fall detection, in order to initiate a control action.

The previous work (Chapter 3) considered the static equilibrium in standing humans, where the upright posture is preserved as long as the person's COM remains above their base of support (BOS) roughly defined by the area covered by the person's feet. A standing person can typically control their center of pressure (COP) to apply restoring moments around their COM projected to the ground to their COM and maintain balance. The boundaries of the BOS are referred to as limits of stability (LOS). Once a person's COM is displaced outside these limits, their COP is unable to apply restoring moments and a fall is initiated. This metric is commonly used to assess the upright balance of a person in quiet standing; however, it does not consider the COM velocity. In motion, dynamic stability should be considered. For example, during sit-to-stand transition the COM resides outside the BOS but is moving towards the BOS with sufficient velocity, and the stability is preserved. On the other hand, a COM moving with excessive velocity might result in a fall, even if currently located within the LOS. The upright posture is preserved if both the COM position and velocity of the person are within certain limits. These dynamic limits were initially derived by Pai et al. [9] using an inverted pendulum model and a state feedback controller with ankle plantar flexor as an input, and further analyzed and tested in [10-12]. Instead of a scalar definition of LOS in quiet standing, the dynamic stability region exists in two-dimensional position-velocity configuration space and will be referred to as a stability basin (SB) throughout this paper. The advantage of this stability metric is that it relies purely on physical states of the person's body, independent of the person's intent. Therefore, the SB of a person

can be estimated offline, knowing the person's mass and height along with typical body proportions and mass distribution, provided by [13], and their LOS. The calculated SB alongside the instantaneous COM states can then be used to predict the onset of a fall.

2.2. Backward falls

Before directly applying the findings from [9], which only considers anterior velocities, several properties of backward falls should be noted. As summarized in Chapter 3, Section 3.1, a person falling backwards has little visual feedback and least effective fall mitigation techniques. The LOS in backward direction is the smallest, meaning there is little room for COP correction before a fall is initiated. In case of an impending fall, a person has two main strategies to prevent an impact with the ground. After the initial delay due to the reaction time, a typical response is an attempt to step in the direction of the fall. However, the effectiveness of such strategy is reduced in the backward direction due to the range of motion of leg joints, which results in the lowest rate of recovery from posterior perturbations, as observed in [14]. The second strategy is described by [15] as a "ballistic" or "impulsive" motion, where the trunk and/or arms are thrown forward to displace the COM to a desired dynamic configuration. Depending on the velocity of the COM, these strategies may be sufficient to recover upright balance. However, due to changes in the visual, vestibular, and musculoskeletal systems associated with older age, elderly people are less successful in utilizing these strategies [16]. Joint range of motion deteriorates as well, resulting in smaller step lengths, further reducing the ability to recover balance [17]. The utility of the impulsive trunk motion is reduced by weakened muscles, and in some cases can be exacerbated by back pains [18].

The factors mentioned above were considered in order to make several assumptions when generating the SB for posterior COM velocities. First, the ankle moments were not considered since they are ineffective in moving the COM once the COP is displaced behind the heels. Second, the impulsive trunk motion was not considered, and the hip angle was assumed to remain largely unchanged throughout the fall. Third, for the initial feasibility exploration of the controller the falling motion was assumed to be in the sagittal plane, since non-sagittal rotation would require changes in

the mechanical design of the device, which is outside the scope of this work; only backward falls are examined in this study. Finally, for the purposes of this paper the COM spatial position and velocity were converted from linear to angular coordinates, i.e., the angle and angular velocity of an imaginary inverted pendulum with its mass concentrated at the body COM and its base located at the heel of the falling person. The angle and angular velocity of this imaginary inverted pendulum will be referred to as the COM angle and (angular) velocity, or COM states, throughout this chapter.

2.3. SB generation

The human body was approximated as a rocking block, described in detail in Chapter 3, Section 5.2. The properties of the block, shown in Table 4-1, were changed from the previous chapter to more closely approximate a human body. The new block, shown in Fig. 4-2, was patterned after a 1.55-m-tall person with a mass of 52 kg. The physical parameters of such person's body were calculated using average kinematic relationships reported by Winter [13], while the LOS were designed after those of an average person, determined by [19-20] as 2.9-4 deg and 5.6-8 deg in the backward and forward direction, respectively. The effort to stabilize the COM with the LOS, typically generated by ankle torques and reactive motion of arms and trunk in humans, was emulated by attaching Velcro strips to the floor and the bottom of the block. Since Velcro engaged only at near-zero angles, it was modeled as a coefficient of restitution (COR) of 0.7, which is similar to the COR used in the previous study.

Figure 4-2. The rocking block experimental apparatus v2 with the CGT v2 attached.

Table 4-1. Comparison of physical parameters of constructed rocking blocks and a human body.

	Block v1	Block v2	Human body
Mass (kg)	54	52	52
Height (m)	-	-	1.55
COM height (m)	0.75	0.87	0.87
Moment of inertia (kg·m^2)	36.2	53	55.5
Forward LOS	7.5	8	5.6-8
Backward LOS	7.5	4	2.9-4

The rocking block model was simulated over a range of initial angles and velocities to construct the inherent SB of the block, presented in Fig. 4-3 in dark gray color. The SB identified by [9] was converted to angular coordinates and is denoted by the red-outlined region for the negative or forward angular velocity on the plot. The

block SB in the forward part of the plot (negative y-axis) is narrower than that of an average person since the block model does not implement any ankle torques to reduce the anterior velocity continuously as opposed to COR, which acts momentarily. However, the top edge of the block SB coincides with the backward fall boundary of the human SB, since ankle torques have limited authority at those configurations.

To calculate the upper boundary of the CGT-assisted SB, the rocking block model was augmented with the model of the thrust generated by the CGT, which was obtained using equations for an isentropic and supersonic flow, described in Chapter 3, Section 9.1. This boundary (dashed line in Fig. 4-3) is defined by the maximum angular velocity at which the block can be returned to upright equilibrium from the given tilt angle. The mathematical derivation is provided in the Section 6.1 of this chapter, while the CGT-expanded SB is graphed in Fig. 4-3 in light gray color. The CGT supervisory controller is implemented by leveraging the region of extended stability computed in this plot; namely, the controller continuously measures the block angle, calculates the maximum angular velocity boundary at that angle, and compares it to the current block angular velocity. When the state configuration of the block approaches the boundary, the controller triggers the CGT, applying the restoring force to the block.

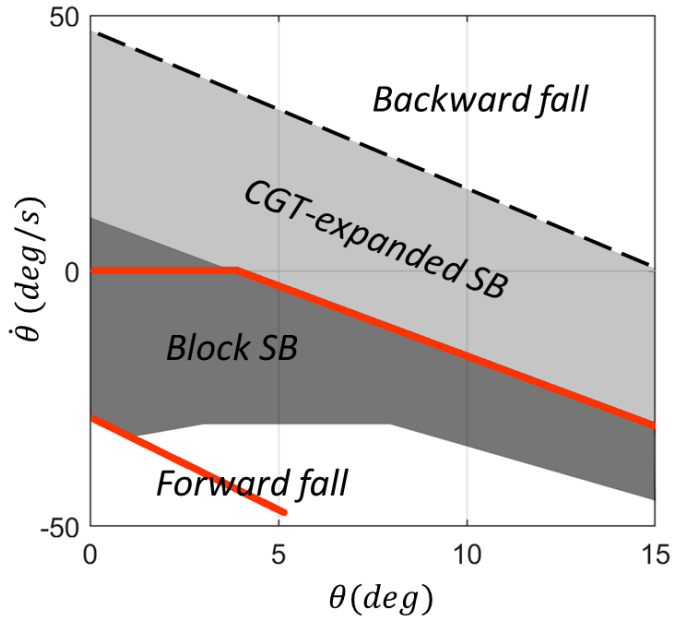

Figure 4-3. Phase plot of the SB of the rocking block apparatus, generated by simulating the rocking block model. The block will settle to equilibrium if configured in its inherent SB (dark gray region); if configured below or above the SB, the block will fall forward or backward, respectively. The light gray band is the CGT-expanded SB, or the region where the CGT can restore the equilibrium to the block. The upper boundary of the CGT-expanded SB is denoted by the dashed line. The red outline defines the the angular representation of the SB found by [9].

3. Experimental Validation

3.1. Experiment protocol

The aim of the conducted experiments was to validate the proposed supervisory controller and assess the control authority of the CGT in case of an impending fall. Two sets of experiments were performed: the first set without the CGT, with an objective to characterize the inherent SB of the rocking block, and the second set with the CGT attached, to verify the expansion of the block SB contributed by the CGT and to assess the supervisory controller performance. During both sets the block started in an upright position. A slack rope was attached to the block to catch it at 35 deg to avoid impact with the floor. At the beginning of each experiment, a researcher pushed the block in the backward direction, imparting different initial angular velocities to the block. In the first set of experiments, the block behavior was recorded and used to identify the inherent

SB of the block. In the second set, the CGT was attached to the block with the nozzle placed at approximately chest level, or 75% of the total height. The nozzle angle was held perpendicular to the pendular axis of the block to enable maximum torque around the corner of the block that contacted the floor. Three reflective markers were attached to the base of the block to measure the tilt angle, and the motion was recorded by a 12-camera motion capture system (Vicon, Oxford GBR) at 200 Hz. The CGT tank was refilled before each experiment in the second set.

The supervisory controller diagram is shown in Fig. 4-4. The controller continuously measured the angle and the angular velocity of the block ($\theta, \dot{\theta}$) using the onboard IMU. Due to the delay in the CGT valve activation, which was approximately 20 ms, the measured states along with the closed-form solution of the linearized block model (Chapter 3, Section 5.3) were used to estimate the states 20 ms into the future ($\theta_f, \dot{\theta}_f$). These estimated states were then used to calculate the maximum allowable velocity $\dot{\theta}_{max}$ that defines the upper boundary of the CGT-expanded SB at θ_f. The CGT remained idle until $\dot{\theta}_f$ exceeded $\dot{\theta}_{max}$, at which point the controller triggered the assistive thrust, returning the block to upright equilibrium. The entire control loop was implemented on an embedded system, described in Chapter 3, Section 4.5, that was attached to the CGT.

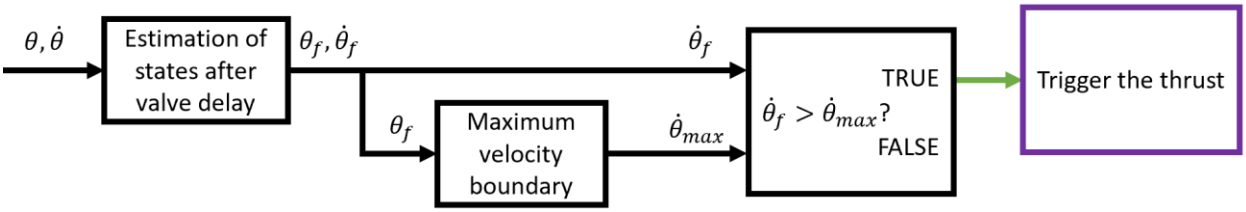

Figure 4-4. The control diagram of the CGT supervisory controller.

3.2. Results

The phase and time plots of the experiment results are shown in Fig. 4-5, top and bottom rows respectively. The initial conditions for both sets, shown as x's on the phase plots, indicate the start events of each experiment, when the researcher's hand was off

the block and no further external input was applied. To identify these events after the data collection, the experiment videos, recorded on a 30 frames per second phone camera, were split into frames using a Python script. The block angle was extracted from the video frames using Unity Engine's UI interface (Unity Technologies, San Francisco CA) and overlaid on the motion capture data to align both data in time. The start events, obtained by observing the video frames, were then transferred to the motion capture data. The thrust events were extracted in a similar fashion to the start events. The embedded system was programmed to switch the color of an onboard LED from green to red once the thrust was commanded. The timing of the thrust events was identified as the instant of this color switch on the experiment videos and transferred to the motion capture angle data and aligned with the video angle data. This process is illustrated in Fig. 4-6, which shows several frames from a representative experiment video.

Without the CGT, the block fell for all initial conditions outside the inherent SB of the block, bounded by the thick black line on the top plots of Fig. 4-5. The red lines represent the experiment trials that resulted in a fall, while green lines are successful recoveries. The magenta dashed line indicates the state evolution of an elderly person from a backward fall video [21] described in the Discussion section of this chapter. The CGT, as shown on the right plots, was able to return the block to its inherent SB by applying a restorative force to the block as it approached the boundary of the CGT-expanded SB. The state trajectories of the CGT-assisted block are colored blue, and the circles indicate the events of thrust. As confirmed by the experiments, the real-time supervisory controller was able to restore upright equilibrium to the block well outside the inherent SB of the block, in conditions which would have resulted in a fall without the CGT assistance.

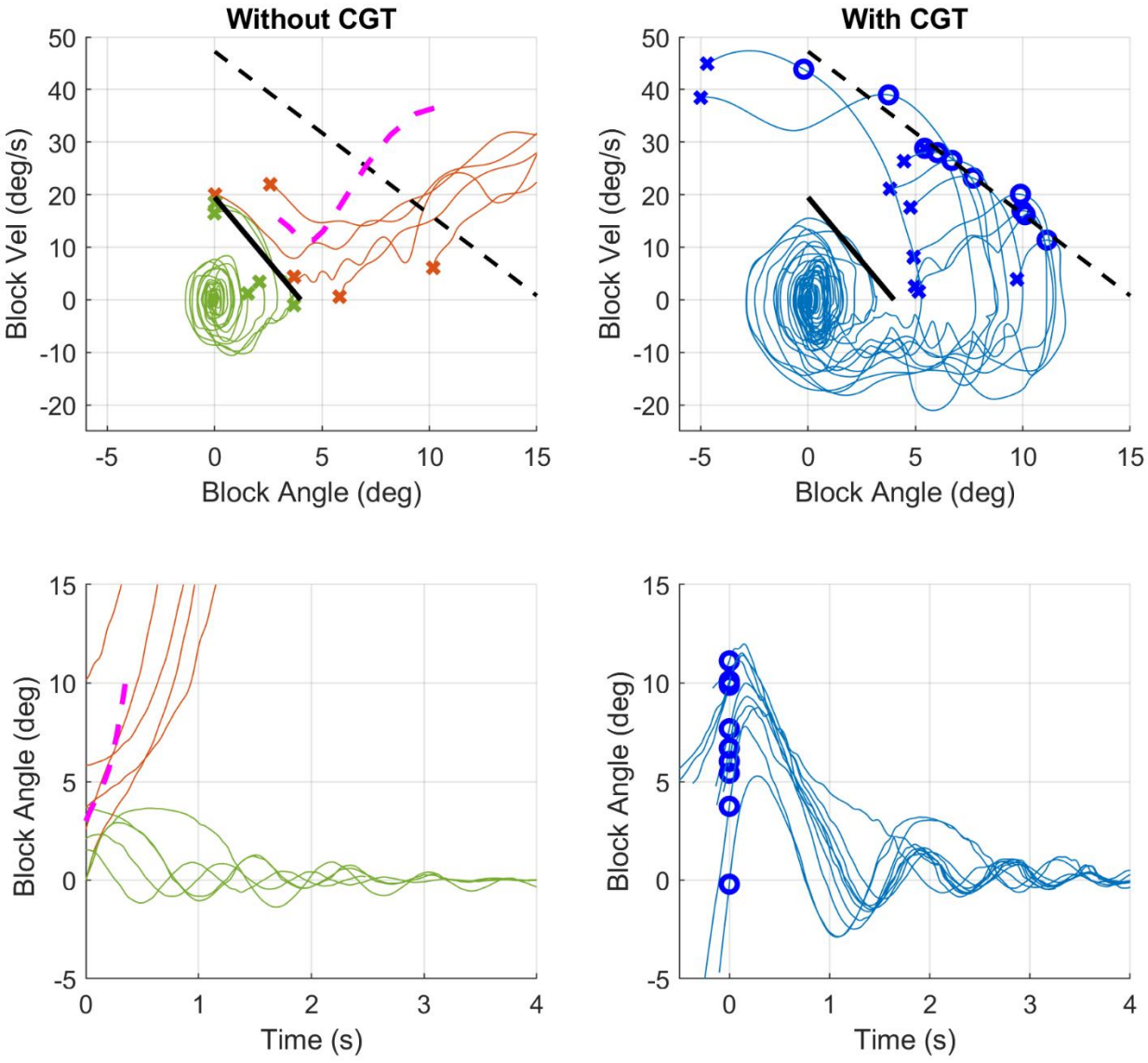

Figure 4-5. Phase plots of the block states (top row) and the block angle vs time (bottom row). Crosses represent the start events of each experiment. Experiments without CGT assistance are plotted on the left, where cases that resulted in upright balance recovery are in green and those that resulted in a fall are in red. The magenta dashed line shows the fall dynamics of an elderly person extracted from a video. Experiments with CGT are on the right in blue, where circles indicate the thrust events. The time axis on the right was adjusted such that the thrust events are aligned for better readability. The solid black line on the phase plots is the block SB boundary and the dashed line is the CGT-expanded SB boundary.

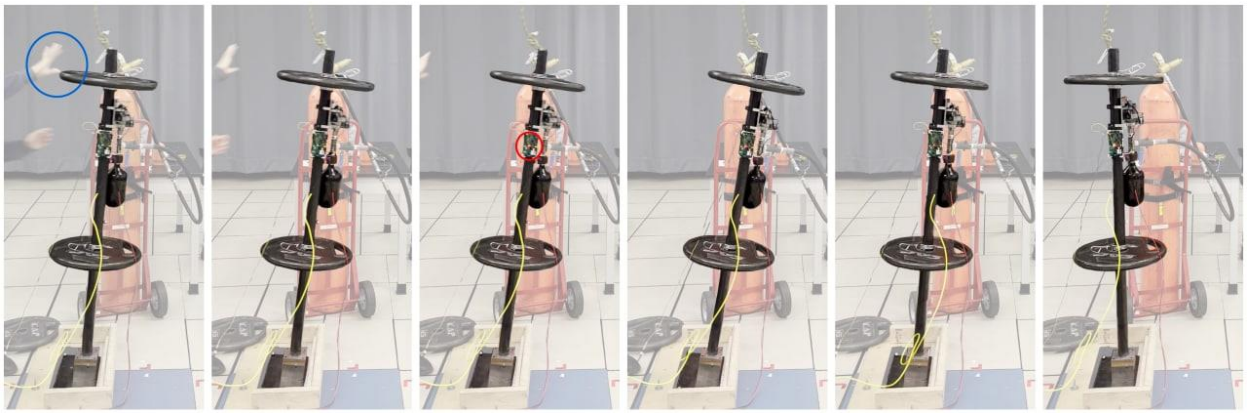

Figure 4-6. Frames from a video of a representative experiment with the CGT attached. Frame 1: researcher has finished pushing, the hand is not contacting the block (blue circle); 2: the block is falling; 3: the thrust has been triggered, onboard LED swithced color from green to red (red circle); 4: the block angular velocity has been brought down to zero; 5: the block returning to its inherent SB; 6: upright equilibrium recovered. The video of the experiments is available at https://youtu.be/1PrSKFisTJs.

4. Discussion

The results of the experiments confirmed the efficacy of the CGT and the robustness of the controller. The rocking block apparatus with the properties of a human body was able to recover the upright equilibrium under the influence of the CGT in dynamic configurations that would normally result in a fall. The controller was able to time the assistance correctly, without imparting insufficient or excessive restorative momentum to the block. However, the rocking block has several key differences with a human body. First, the rocking block is predominantly rigid, while a human body consists of several segments connected by joints. While a straight body configuration can be approximated by a block fairly accurately, sufficiently large joint angles can change the body moment of inertia and the length of the equivalent pendulum. As such, the rocking block experiments might not be sufficient to confidently validate the reliability of the supervisory controller for different fall configurations. Second, the response of the body in non-straight configuration to an assistive thrust is unclear, since the thrust might impart significant momentum to the trunk segment it is affixed to, without this momentum necessarily propagating to the entire body. Third, the IMU affixed to the CGT in the backpack form measures the trunk angle. The COM angle with

respect to the inertial frame of reference, while approximately equal to the trunk angle for a straight body configuration, may diverge from the trunk angle for sufficiently large joint angles. For estimating the correct nozzle angle, at which the assistive thrust is applied, the COM angle is necessary. As such, two questions may be posed to further examine the validity of these experiments as it relates to human use:

- To what extent does the rocking block (single-link pendulum) model reflect the multi-link dynamics of a falling person?
- How closely does the IMU-measured trunk angle represent the COM angle required by the controller?

4.1. OpenSim simulations

To help inform these questions, the human body response to the CGT assistance in non-straight configurations was assessed through an exploratory simulation. The simulation was performed in OpenSim [22-23] software, commonly used in the study of biomechanics. In this simulation, the human body was represented as a three-link pendulum, where the top link is the head-arms-trunk (HAT) segment, the middle link is the leg segment, and the bottom link is the foot segment. The model was intended to represent a 1.55-m 52-kg person. The lengths, masses, and moments of inertia of the links were selected based on the average human body proportions and mass distributions presented by [13]. The foot segments were fixed to the ground. The ankle and hip joints were modeled as rotary joints with ideal torque generators governed by internal PD controllers. The goal of the ankle controller was to regulate the COM angle to zero, while the hip controller maintained the trunk in desired poses as described below. The joint torque limits were taken from literature describing typical joint torques for the elderly population. Specifically, the ankle torque was limited to 22 Nm per leg (44 Nm total) [24] and the hip torque was limited to 51 Nm per leg (102 Nm total) [25].

The simulation was performed for three poses: a “straight body” pose, which is the closest configuration to the rocking block, where the trunk axis was aligned with leg axis; a “vertical trunk” pose, where the trunk axis was aligned with the ground vertical; and a “hunched forward” pose, where the hip joints remained fixed at a non-zero angle

(40 deg in this study), such that the trunk axis was offset from the leg axis. The latter two poses were selected as common modes of backward falling, based on several videos of such falls recorded in elderly care facilities [21, 26]. The poses are sketched on the bottom row of Fig. 4-7 as stick figures, the transparent sketch representing the upright equilibrium (zero COM angle) and the solid sketch representing the COM state configuration denoted by the blue square in the corresponding phase plots in the top row. Each pose was simulated at different initial conditions to identify the inherent SB for the body COM, which is defined by the ability of the model to return to upright equilibrium with the help of the ankle torques. The COM states (angle and angular velocity) were extracted from the segments motion and plotted on the top row of Fig. 4-7, with successful balance recovery cases plotted in green and fall cases in red. The backward LOS of 4 deg is denoted by the solid black line, to the left of which the model can reduce the backward velocity with ankle dorsiflexors, while to the right of it the model has no means of preventing the fall.

4.2. Single-link block and multi-segment body comparison

The inherent and CGT-expanded SBs of the rocking block are plotted in thin and thick dashed lines respectively. The plots indicate that the rocking block inherent SB is similar to the human body model SB, with slight variations for different poses. The COM state trajectories in the phase plot follow the same trends as the rocking block states in Fig. 4-5. This suggests that even if the rocking block is a single rigid body as opposed to multi-segment structure of a human body, it might be a sufficient approximation of the human body COM in regard to detecting imbalance in the backward direction.

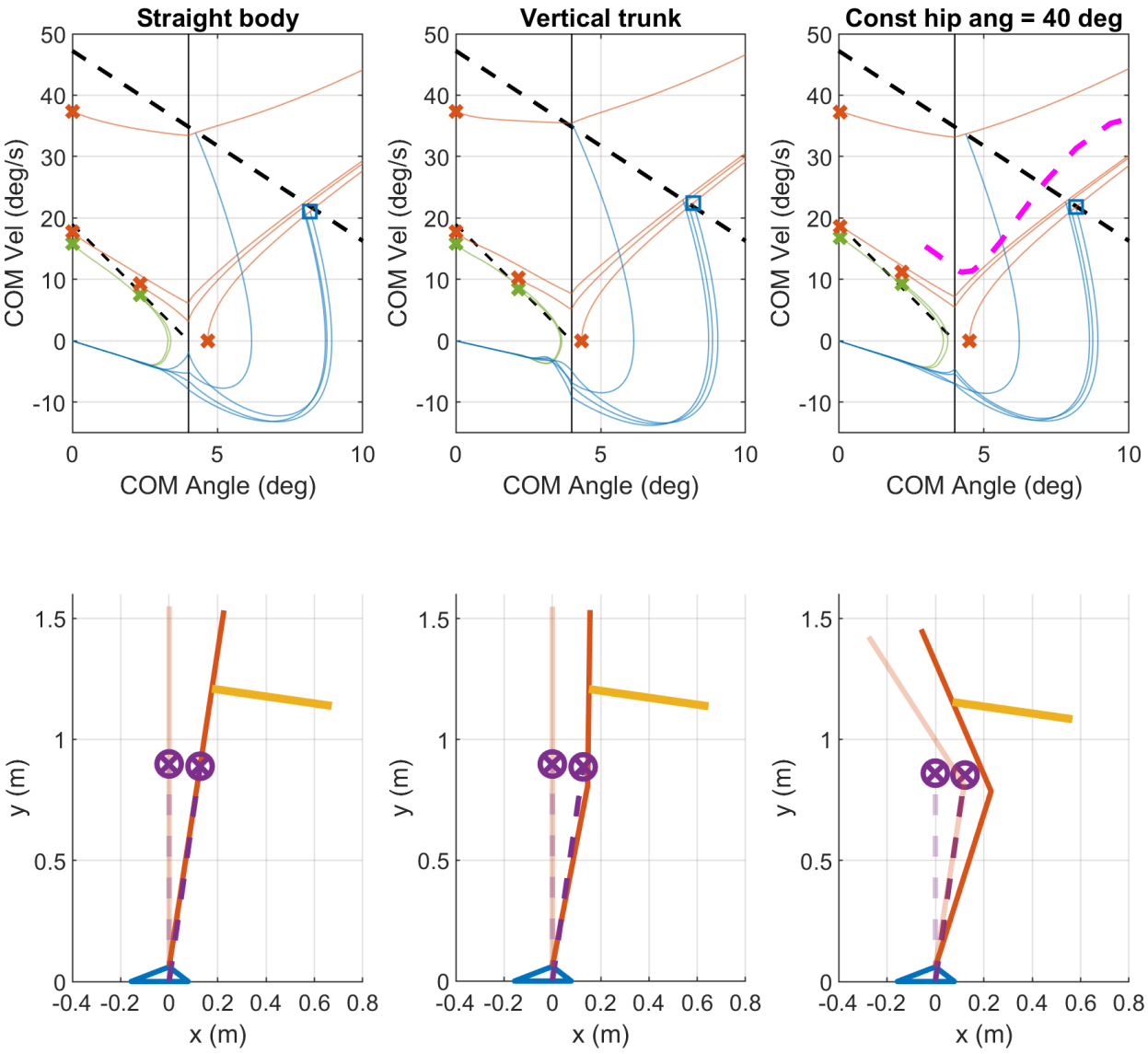

Figure 4-7. Results of an OpenSim simulation of a two-link pendulum model of a human falling backwards. The top row displays the state evolutions of the COM from different initial conditions. Green lines represent the cases where the pendulum returned to equilibrium, while the red lines show the cases resulting in a fall. The blue lines show how the equilibrium is recovered by the CGT assistance. The bottom row depicts the poses of the modeled human, where (a) trunk is aligned with legs, (b) trunk is aligned with the ground vertical, and (c) trunk is kept constantly offset from legs. The nozzle in orange is oriented perpendicularly to the COM vertical.

Consequently, an assistive thrust was applied to the model at the point where the CGT would be worn. The nozzle was located on the HAT segment at 1.16 m height, approximately 75% of the person's height. The thrust profile was created using the thrust model, described in Chapter 3, Section 9.1. The same control algorithm from the

experiments was applied. The thrust was triggered at the moment when the COM states of the body model crossed the upper boundary of the CGT-expanded SB. The nozzle (the orange vector in Fig 4-7, bottom row) was oriented perpendicularly to the COM vertical axis for maximum restorative moment around the heel of the modeled human. For all such cases, the upright equilibrium was restored to the body. Therefore, the supervisory controller correctly timed the intervention, so that the applied assistance was neither insufficient nor excessive, which confirms that the COM states (that the rocking block model approximates) provide sufficient information for the controller. The momentum imparted by the CGT to the trunk was successfully transferred to the body COM through the hips at all poses. In the multi-segment body model, governed by internal joint controllers with realistic limits, response dynamics similar to those of a rocking block were observed, which indicates that a human user would benefit from the presented mode of assistance in a form of a force impulse. Similar results were observed in the cursory backward fall experiment presented in Chapter 3, Section 3.2, although that experiment was performed only on a "straight body" pose.

To ground the simulations to real-world fall scenarios, they were compared to a real human backward fall. The authors could not locate any studies with information on the body COM position during falls. COM information was instead extracted using a frame-by-frame 3D analysis from one of the videos of backward falls [21]. A frame from the video (Fig. 4-8) shows the subject in hunched forward pose using a walker mid-backward fall. The focal length and the spatial position of the camera used to record the video was extracted using an open-source software fSpy (Stuffmatic, Stockholm, Sweden). The extracted information was used to reconstruct the scene in 3D space in Blender, an open-source 3D modeling software (Blender Foundation, Amsterdam, Netherlands) and then imported to Unity Engine. The video frames were overlayed on the 3D UI of the engine, and the falling person's silhouette was tracked in 3D space with a four-segment (foot, shank, thigh, and HAT) object, as shown in Fig. 4-8. The positions and orientations of the segments, along with the nominal segment mass distribution [13], were used to calculate the COM angle in the sagittal plane, which was then differentiated to obtain the COM angular velocity, in MATLAB. The state evolution of the

falling person from the video is plotted on Fig. 4-5 and 4-7 as a dashed magenta line. Although the video subject attempts to use the walker to break the fall and their mass is unknown, the state evolution is similar to that of the simulation and the rocking block experiments, which further supports the hypothesis that the rocking block dynamics might be a valid approximation for the dynamics of the human body COM.

Figure 4-8. A frame from a video recording of a resident of an elderly care facility [21] during a backward fall with the 3D matching procedure overlayed.

4.3. COM angle estimation

The final concern is the estimation of the user's body COM angle and angular velocity, which is not a trivial problem for a portable device. Since the onboard IMU measures the trunk angle, the controller receives a reliable COM angle only when the trunk vertical is mostly aligned with the COM vertical, i.e., a straight body pose. For a vertical trunk pose, the IMU will read the angle and angular velocity as zero. For hunched forward pose the angle measurements will be biased in the anterior direction. However, the IMU-measured trunk linear acceleration in all axes can potentially be integrated to access the linear spatial velocity information, which can be used to estimate the COM angle and angular velocity for small angles. Such estimation, the derivation of which is provided in Section 6.2 of this chapter, was tested on some of the simulation cases presented earlier. Only the parts of the studied trajectories outside the LOS ($\theta_{COM} > 4$

deg) were considered. The comparison between the actual (red solid lines) and estimated (purple dashed lines) is shown in Fig. 4-9 for the three poses. The circles of corresponding colors indicate the events of the thrust application. The stars show the actual COM states at the moment the thrust would be triggered if only IMU signals informed the time of intervention. The estimated COM angle and angular velocity are fairly close to the actual values, and, more importantly, the intervention would be triggered prior to the moment when the COM states leave the CGT control authority. While applying assistance earlier is suboptimal, since more than the necessary minimum impulse is imparted to the falling body, it nonetheless results in a successful fall prevention. The body response to the assistance was simulated using the triggering event based exclusively on IMU information and plotted in Fig. 4-9 as blue lines. The COM is pushed forward further than in Fig. 4-7, but never leaves the LOS, and upright equilibrium is achieved.

However, even though the IMU signals alone have potential to be sufficient for informing the CGT assistance, there might be cases when the user has already initiated or performed a step backwards to prevent the backward fall or when the backward motion is intentional, such as sitting down or leaning against a wall. The controller should account for such edge cases in the activities of daily living. To collect this additional information, the CGT can be instrumented with several supplementary sensors. Legs motion could be estimated with goniometers measuring knee and ankle joint angles or additional IMUs measuring the thigh and shank absolute angles. The sitting or leaning intent could be inferred with a backward facing depth camera, which could be also used to assess particularly dangerous situations, such as when the user is at the top of a staircase, to add a factor of safety to the controller when necessary. The combination of these additional sensors could also improve the accuracy of the COM state measurements. The extent to which such additional sensing might be needed is a topic of future work.

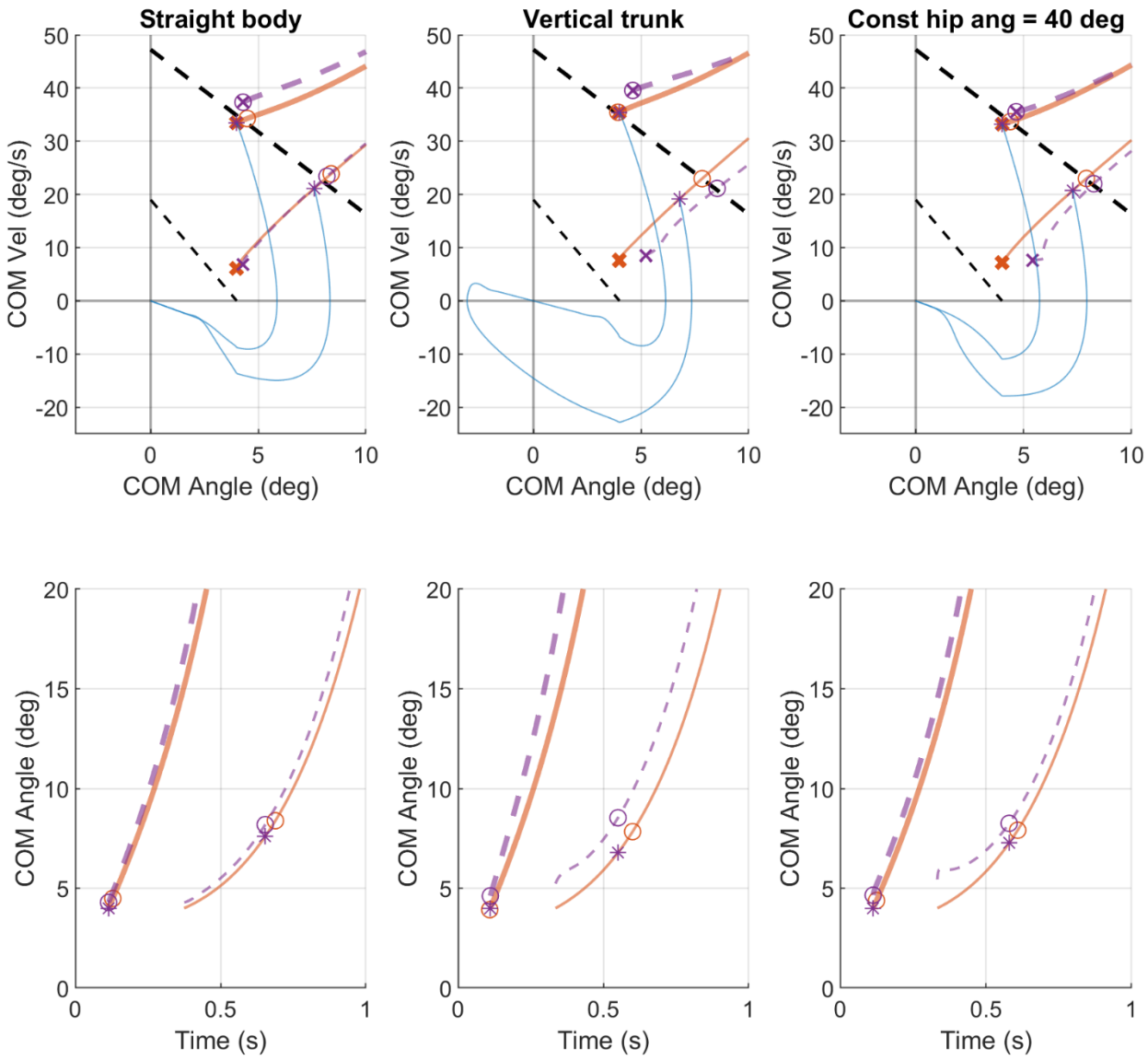

Figure 4-9. Comparison of the COM state trajectories (red solid) and their counterparts estimated using exclusively trunk IMU signals (purple dashed). The top and bottom rows show the phase and time plots. Circles indicate the crossings of the upper boundary of the CGT-expanded SB. The stars indicate the states at the moment the assistive thrust would be applied if the CGT controller only used trunk IMU signals. The blue lines depict the COM states trajectory after the assistive thrust was applied.

The control diagram shown in Fig. 4-4 would need to be expanded for human use, as depicted in Fig. 4-10. The COM angle and velocity $(\theta, \dot{\theta})$ will be computed from the CGT sensors, then the future states after the valve delay $(\theta_f, \dot{\theta}_f)$ will be calculated using the closed form solution of the rocking block equation of motion. The future tilt angle will be used to calculate the maximum allowable velocity $\dot{\theta}_{max}$, described in the

Experimental protocol section of this chapter. If the $\dot{\theta}_f$ is below this limit, the nozzle angle would be continuously modulated to orient the thrust vector perpendicularly to the COM vertical axis in anticipation of a potential fall. Once $\dot{\theta}_f$ exceeds $\dot{\theta}_{max}$, the CGT would trigger the assistive thrust to return the user to upright equilibrium. The implementation of a human-wearable CGT prototype is a subject of future work.

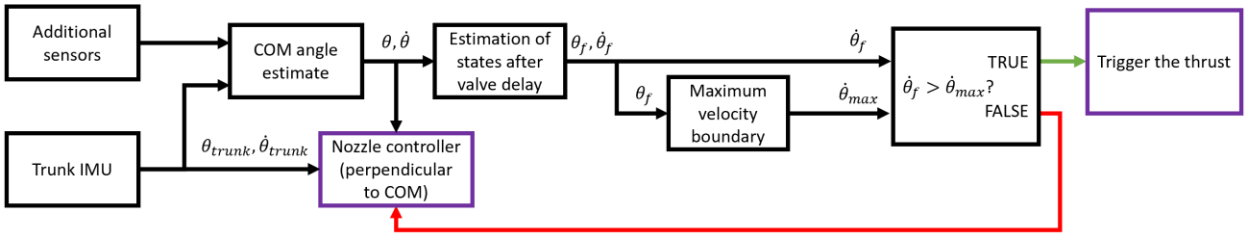

Figure 4-10. The control diagram of the CGT supervisory controller for a human-wearable version.

5. Conclusion

This chapter described the supervisory controller for the CGT responsible for detecting backward falls early in fall initiation and determining when to apply the assistive thrust to recover the upright equilibrium to the potential user. The feasibility of such a controller was tested on a rocking block experimental apparatus. As the experiment results indicate, the CGT expanded the stability basin of the block significantly, thereby reducing the likelihood of falling. The model-based supervisory controller was able to accurately predict the correct boundary of the CGT control authority and apply the assistive thrust on timely fashion, successfully recovering upright stability to the block for all experiment trials.

The rocking block model assumptions in approximating a human body were noted. A simulation of a three-segment (foot, leg, HAT) physical model with joints actuated under biomimetic torque limits was constructed in OpenSim software and performed for three trunk poses (straight body, vertical trunk, hunched forward). The results of the simulations suggest that different poses do not significantly affect the CGT control authority limits. Thus, a rocking block model might be a sufficient representation

of a human body COM for the supervisory controller, especially given the small angles at which the CGT operates.

Finally, some remarks were provided about instrumentation of the CGT to correctly measure the COM angle and angular velocity. A COM angle estimation method was proposed that uses IMU signals to derive COM angle and angular velocity for small angles. Simulations where the controller only had access to COM states estimated with the proposed method were performed, and the results indicated that in such conditions, the CGT behaves more conservatively and intervenes earlier; however, the assistive thrust, while applied not at the boundary of the CGT control authority, does not result in excessive forward momentum.

The study presented in this chapter concludes the feasibility exploration of the CGT based fall prevention device. Although it was limited by several assumptions, the constructed prototype and the supervisory controller significantly expanded the stability basin of the completely passive rocking block experimental apparatus, thus showing promise to substantially assist a human user in preventing backward falls. Given the fact that the CGT intervenes early in the fall, such assistance may range from reversing falls and returning the user to upright equilibrium to reducing the backward velocity and increasing the time window for the user to recover from imbalance. Further investigation will include testing of the CGT and the controller with human participants, which will inform the necessary instrumentation of the CGT and possible changes to the controller.

6. Addendum

6.1. The upper boundary of the CGT-expanded SB.

The behavior of the block tilted at an angle of θ under the influence of the CGT was described in Chapter 3, Section 5.2 by the following equation of motion:

$$\ddot{\theta}(t) = \frac{mgl}{I}\sin(\theta(t) - sign(\theta(t))\alpha) - \frac{R}{I}F(t), \quad (1)$$

where the moment of inertia and mass of the block are denoted by I and m, g is the gravity constant, F is the magnitude of the force applied by the CGT to the block at height R, and α is the slenderness angle, which can also be interpreted as the LOS, of the block. Since a falling block does not cross zero, thus not experiencing a rocking motion, the signum function can be omitted, and the block is equivalent to a pendulum of length l with its base located at the contact point of the corner of the block with the floor and its mass concentrated at the block COM. The pendulum angle q can then substitute the quantity $\theta - \alpha$, and to obtain the closed form solution the sine function can be linearized around an operating point q_L. After plugging in the thrust model, the equation of motion of the equivalent pendulum is

$$\ddot{q}(t) = \frac{1}{I}\Big(mgl\cos q_L\, q(t) + mgl(\sin q_L - q_L \cos q_L) - RF_{max}e^{-\frac{t}{\tau}}\sin(\beta)\Big), \tag{2}$$

where F_{max} and τ are the thrust amplitude and time constant, and β is the nozzle angle with respect to the equivalent pendulum. Using the closed form solution of (2) and the nozzle angle of 90 deg, the block maximum angular velocity $\dot{\theta}_{max} = \dot{q}_{max}$ from which the CGT can help recover upright balance can be expressed as

$$\dot{q}_{max}(q_0) = -H(C_1 + C_2), \tag{3}$$

where

$$H = \sqrt{\frac{mgl\cos q_L}{I}}, \tag{4}$$

$$C_1 = \frac{B_2}{H\tau}, \tag{5}$$

$$C_2 = \frac{B_1 + B_2 e^{-\frac{t}{\tau}} + B_3\cosh(Ht_{end})}{\sinh(Ht_{end})}, \tag{6}$$

with t_{end} being the duration of the CGT thrust (approximately 0.7 s) and

$$B_1 = q_L - \tan q_L, \tag{7}$$

$$B_2 = -\frac{RF_{max}}{I(\tau^{-2} - H^2)}, \tag{8}$$

$$B_3 = q_0 - B_1 - B_2. \tag{9}$$

6.2. Estimation of COM angle and angular velocity from IMU signals.

Figure 4-11 depicts a two-link pendulum approximating a human body. The top link is the trunk segment, while the bottom link is the leg segment. The body COM is nominally located at 56% of the total height, or near the proximal end of the trunk segment. As such, the top link length, l_1, is 3% of the total height, while the bottom link length, l_2, is 53% of the total height [13]. The length of the line from the ground support point to the COM is l_{COM}. The IMU is located at the position of the COM is denoted by (x_{COM}, y_{COM}). Since the CGT is expected to apply the assistive thrust early in the fall, the COM and segment angles can be assumed to be small. Using the small angles assumption, the COM linear position and velocity can be approximated by:

$$x_{COM} = l_1\theta_1 + l_2\theta_2 = l_{COM}\theta_{COM} \tag{10}$$

$$y_{COM} = l_1 + l_2 = l_{COM} \tag{11}$$

$$\dot{x}_{COM} = l_1\dot{\theta}_1 + l_2\dot{\theta}_2 = l_{COM}\dot{\theta}_{COM} \tag{12}$$

$$\dot{y}_{COM} = -l_1\theta_1\dot{\theta}_1 - l_2\theta_2\dot{\theta}_2 = -l_{COM}\dot{\theta}_{COM}\theta_{COM} \tag{13}$$

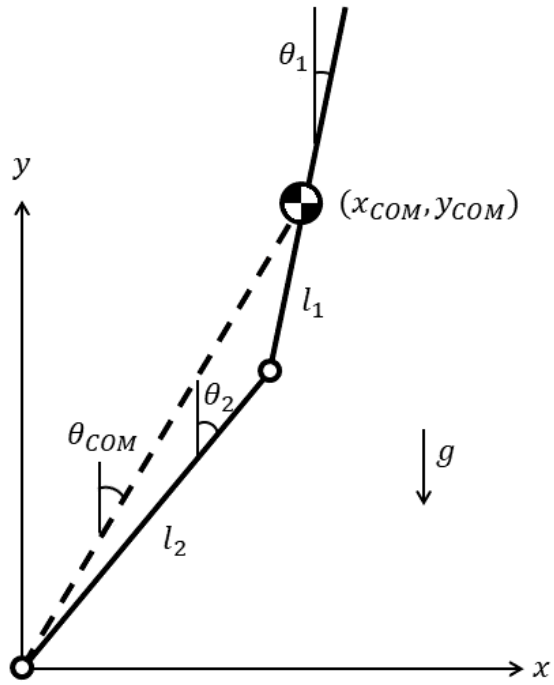

Figure 4-11. Free-body diagram of a two-link pendulum representing a human body.

This IMU measures the trunk linear accelerations, $\ddot{x}_{COM}, \ddot{y}_{COM}$, which can be used to determine the trunk angle θ_1 and angular velocity $\dot{\theta}_1$. Assuming that these accelerations can be integrated to obtain the linear velocity of the IMU, $\dot{x}_{COM}, \dot{y}_{COM}$, the bottom link angle θ_2 can be calculated from (12) and (13) as:

$$\theta_2 = \frac{\dot{y}_{COM} + l_1 \dot{\theta}_1 \theta_1}{l_1 \dot{\theta}_1 - \dot{x}_{COM}} \tag{14}$$

Finally, knowing θ_2 and using (10) and (12), the COM angle θ_{COM} and angular velocity $\dot{\theta}_{COM}$ can be approximated as:

$$\theta_{COM} = \frac{1}{l_{COM}} (l_1 \theta_1 + l_2 \theta_2) \tag{15}$$

$$\dot{\theta}_{COM} = \frac{1}{l_{COM}} \dot{x}_{COM} \tag{16}$$

7. References

[1] M. Mubashir, L. Shao, and L. Seed, “A survey on fall detection: Principles and approaches,” *Neurocomputing*, vol. 100, pp. 144–152, 2013.

[2] N. Noury et al., "Fall detection - Principles and Methods," *2007 29th Annual International Conference of the IEEE Engineering in Medicine and Biology Society*, 2007, pp. 1663-1666, doi: 10.1109/IEMBS.2007.4352627.

[3] M. Dedabrishvili, B. Dundua, and N. Mamaiashvili, “Smartphone sensor-based fall detection using machine learning algorithms,” *Advances and Trends in Artificial Intelligence. Artificial Intelligence Practices*, pp. 609–620, 2021.

[4] J. Chen, K. Kwong, D. Chang, J. Luk and R. Bajcsy, "Wearable Sensors for Reliable Fall Detection," *2005 IEEE Engineering in Medicine and Biology 27th Annual Conference*, 2005, pp. 3551-3554, doi: 10.1109/IEMBS.2005.1617246.

[5] M. Kangas, A. Konttila, P. Lindgren, I. Winblad, and T. Jämsä, “Comparison of low-complexity fall detection algorithms for body attached accelerometers,” *Gait & Posture*, vol. 28, no. 2, pp. 285–291, 2008.

[6] K. de Miguel, A. Brunete, M. Hernando, and E. Gambao, “Home camera-based fall detection system for the elderly,” *Sensors*, vol. 17, no. 12, p. 2864, 2017.

[7] R. Planinc and M. Kampel, “Introducing the use of depth data for fall detection,” *Personal and Ubiquitous Computing*, vol. 17, no. 6, pp. 1063–1072, 2012.

[8] M. N. Nyan, F. E. H. Tay, and E. Murugasu, “A wearable system for pre-impact fall detection,” *Journal of Biomechanics*, vol. 41, no. 16, pp. 3475–3481, 2008.

[9] Y.C. Pai and J. Patton, “Center of mass velocity-position predictions for balance control,” *Journal of Biomechanics*, vol. 30, no. 4, pp. 347–354, 1997.

[10] J. Patton, Y.C. Pai, and W. Lee, “Evaluation of a model that determines the stability limits of dynamic balance,” *Gait and Posture*, vol. 9, no. 1, pp. 38-49, 1999, doi: 10.1016/s0966-6362(98)00037-x.

[11] A. L. Hof, M. G. J. Gazendam, and W. E. Sinke, "The condition for dynamic stability," *Journal of Biomechanics*, vol. 38, no. 1, pp. 1-8, 2005, doi: 10.1016/j.jbiomech.2004.03.025.

[12] M. Simoneau and P. Corbeil, "The effect of time to peak ankle torque on balance stability boundary: experimental validation of a biomechanical model," *Experimental brain research*, vol. 165, no. 2, pp. 217–228, 2005, doi: 10.1007/s00221-005-2290-1.

[13] D. A. Winter, *Biomechanics and Motor Control of Human Movement*, vol. 7., Hoboken, NJ, USA: John Wiley & Sons, Inc., 2009.

[14] E. T. Hsiao and S. N. Robinovitch, "Common protective movements govern unexpected falls from standing height," *Journal of biomechanics*, vol. 31, no. 1, pp. 1-9, 1998, doi: 10.1016/s0021-9290(97)00114-0.

[15] Y. Suzuki, T. Nomura, M. Casadio, and P. Morasso, "Intermittent control with ankle, hip, and mixed strategies during quiet standing: a theoretical proposal based on a double inverted pendulum model," *Journal of theoretical biology*, vol. 310, pp. 55–79, 2012, doi: 10.1016/j.jtbi.2012.06.019.

[16] M. B. King, J. O. Judge, L. Wolfson, "Functional base of support decreases with age," *Journal of Gerontology*, vol. 49, no. 6, pp. M258-63, 1994, doi: 10.1093/geronj/49.6.m258.

[17] B. E. Maki, W. E. McIlroy, and G. R. Fernie, "Change-in-support reactions for balance recovery," *IEEE Engineering in Medicine and Biology Magazine*, vol. 22, no. 2, pp. 20-26, 2003, doi: 10.1109/MEMB.2003.1195691.

[18] N. W. Mok, S. G. Brauer, and P. W. Hodges, "Hip strategy for balance control in quiet standing is reduced in people with low back pain," *Spine*, vol. 29, no. 6, pp. E107–E112, 2004, doi: 10.1097/01.brs.0000115134.97854.c9.

[19] B. Brouwer, E. G. Culham, R. A. L. Liston, and T. Grant, "Normal variability of postural measures: Implications for the reliability of relative balance performance outcomes," *Scandinavian Journal of Rehabilitation Medicine*, vol. 30, no. 3, pp. 131–137, Sep. 1998, doi: 10.1080/003655098444048.

[20] N. T. Shepard, “Interpretation and Usefulness of Computerized Dynamic Posturography,” *Vestib. SIG*, no. Winter 2015/2016, pp. 18–30.

[21] S. N. Robinovitch, F. Feldman, Y. Yang, R. Schonnop, P. M. Leung, T. Sarraf, J. Sims-Gould, and M. Loughin, “Video capture of the circumstances of falls in elderly people residing in long-term care: an observational study,” *Lancet*, vol. 381, no. 9860, pp. 47–54, 2013, doi: 10.1016/S0140-6736(12)61263-X.

[22] A. Seth, J. L. Hicks, T. K. Uchida, A. Habib, C. L. Dembia, J. J. Dunne, C. F. Ong, M. S. DeMers, A. Rajagopal, M. Millard, S. R. Hamner, E. M. Arnold, J. R. Yong, S. K. Lakshmikanth, M. A. Sherman, J. P. Ku, and S. L. Delp, “Opensim: Simulating musculoskeletal dynamics and neuromuscular control to study human and animal movement,” *PLOS Computational Biology*, vol. 14, no. 7, 2018.

[23] S. L. Delp, F. C. Anderson, A. S. Arnold, P. Loan, A. Habib, C. T. John, E. Guendelman, and D. G. Thelen, “OpenSim: Open-source software to create and Analyze dynamic simulations of movement,” *IEEE Transactions on Biomedical Engineering*, vol. 54, no. 11, pp. 1940–1950, 2007.

[24] D. G. Thelen, A. B. Schultz, N. B. Alexander, and J. A. Ashton-Miller, “Effects of age on rapid ankle torque development,” *The journals of gerontology, Series A, Biological sciences and medical sciences*, vol. 51, no. 5, pp. M226–M232, 1996, doi: 10.1093/gerona/51a.5.m226.

[25] T. D. Cahalan, M. E. Johnson, S. Liu, and E. Y. Chao, “Quantitative measurements of hip strength in different age groups,” *Clinical orthopaedics and related research*, no. 246, pp. 136–145, 1989.

[26] W. J. Choi, J. M. Wakeling, and S. N. Robinovitch, “Kinematic analysis of video-captured falls experienced by older adults in long-term care,” *Journal of biomechanics*, vol. 48, no. 6, pp. 911–920, 2015, doi: 10.1016/j.jbiomech.2015.02.025.

CHAPTER 5

CONCLUSION

This dissertation has presented feasibility explorations of two human-oriented assistive mechatronic devices: the Swing Assist (SA) knee prosthesis and the Cold-Gas Thruster (CGT) based fall prevention device. The SA knee is a lightweight and low-impedance device that can actively assist the user during locomotion. This device relies on passive stance knee stability, while utilizing a small motor to inject power in swing phase only as needed. This package combines the advantages of passive (light weight and low output impedance) and powered (active assistance to ensure full extension at heel strike and good disturbance rejection) prostheses. The device prototype was tested on an individual with transfemoral amputation and was shown to improve the swing consistency and repeatability both stride-to-stride and across all walking speeds while also reducing the user's hip effort, compared to the daily-use prosthesis.

The CGT is intended as a prospective fall prevention device that utilizes compressed gas to generate a restorative thrust to help restore balance upon detection of the onset of a fall. The constructed prototype consists of a commercially available high-pressure tank, an electronically controlled custom-made valve with high-flow capacity, and a converging-diverging nozzle, that are employed together to generate a thrust pulse with a magnitude of 370 N. A rocking block experimental apparatus with the dynamic parameters (mass, moment of inertia, and COM height) of a 54-kg 1.55-m-tall human body was constructed to assess the control authority of the CGT. A real-time autonomous supervisory controller was developed to track the angle and angular velocity of the block to detect initiated falls. The controller utilizes these measured states along with the physical models of the rocking block and the thruster to trigger the valve, releasing the compressed gas from the tank that generates an assistive thrust, which returns the block to upright stability. The CGT control authority limits were identified through a series of experiments. The assumptions and limitations of the

experiments were discussed, and additional simulations were performed to explore the effects of the CGT on a multi-segment human body model. Based on the results of the experiments and simulations, it can be concluded that the CGT has the potential to prevent backward falls and significantly expand the margins of stability of its user. Future work will involve implementing the suggested changes to the CGT instrumentation and the controller for human use; designing a human-CGT interface in the form of a wearable backpack; and testing the efficacy of the CGT and the control approach on human participants.